3-21-2013

Passive, Low Cost Neutron Detectors for Neutron Diagnostics at the National Ignition Facility

Nathaniel C. Loyd

PASSIVE, LOW COST NEUTRON DETECTORS FOR NEUTRON DIAGNOSTICS AT THE NATIONAL IGNITION FACILITY

THESIS

Nathaniel C. Loyd, First Lieutenant, USAF
AFIT-ENP-13-M-23

DEPARTMENT OF THE AIR FORCE
AIR UNIVERSITY

AIR FORCE INSTITUTE OF TECHNOLOGY

Wright-Patterson Air Force Base, Ohio

The views expressed in this thesis are those of the author and do not reflect the official policy or position of the United States Air Force, Department of Defense, or the United States Government.

AFIT-ENP-13-M-23

PASSIVE, LOW COST NEUTRON DETECTORS FOR NEUTRON DIAGNOSTICS AT THE NATIONAL IGNITION FACILITY

THESIS

Presented to the Faculty

Department of Engineering Physics

Graduate School of Engineering and Management

Air Force Institute of Technology

Air University

Air Education and Training Command

In Partial Fulfillment of the Requirements for the

Degree of Master of Science in Nuclear Engineering

Nathaniel C. Loyd, BS

First Lieutenant, USAF

March 2013

DISTRIBUTION STATEMENT A.
APPROVED FOR PUBLIC RELEASE; DISTRIBUTION UNLIMITED

AFIT-ENP-13-M-23

PASSIVE, LOW COST NEUTRON DETECTORS FOR NEUTRON DIAGNOSTICS AT THE NATIONAL IGNITION FACILITY

Nathaniel C. Loyd, BS

First Lieutenant, USAF

Approved:

Dr. John W. McClory (Chairman)	11 MAR 2013 Date
Maj Benjamin R. Kowash, USAF, PhD (Member)	8 Mar 2013 Date
Dr. Abigail A. Bickley (Member)	3/5/2013 Date

Abstract

Experimental validation of neutron fluence models of fusion events at the National Ignition Facility is necessary to predict radiation damage to measurement electronics. Due to programmatic and facility limitations, traditional neutron measurement techniques are not well suited for this application. Notably, a low cost and passive measurement technique that provides a permanent record is preferred. A detector was designed using gadolinium oxide contained within an aluminum reservoir. The reservoir is secured by a thin layer of Mylar and x-ray film, and vacuum sealed in a light tight package. In the presence of a thermal neutron flux, the gadolinium atoms absorb incident neutrons and partially de-excite by conversion electron emission. The conversion electrons exit the gadolinium oxide layer, penetrate the Mylar, and expose the x-ray film. After developing the film, the film exposure is quantified and directly related to the neutron fluence. The configuration was sensitive to thermal neutron fluences between 1.43×10^{7} and 1.43×10^{9} n/cm^2, and could distinguish between fluences differing by more than a tenth of a decade.

Vita, Dulcedo, Spes

Acknowledgements

I am the unworthy recipient of assistance far beyond what I deserve. I hope that readers of this humble work first see this, so that I may not retain any undue credit.

First, I thank my committee. Dr. Abigail Bickley and Major Benjamin Kowash provided indispensible guidance from inception to completion of this research. I am indebted to their wisdom and expertise. I also thank Dr. John McClory. Patient, sagacious, and more dedicated than any professor I've ever encountered, he enabled me to complete this work, encouraged me professionally, and after proofing nearly a thousand pages of other theses, was able to give meaningful advice to help make this document what it is. I hope that my work gives credit to his name.

I thank my beautiful, precious wife. She patiently suffered sleepless nights, sick children, and an absent husband, yet, harrowed from long days, still provided a happy home for my return. I love you eternally. I also thank my sons. My life would be vapid without you, and your laughter (and crying) brings light to even the darkest days.

Finally, and most importantly, this work is dedicated to the immaculate mother of God, for whom it was performed. I give it all, my puerile macaroni art, to my mother as an expression of my love. In giving my patroness this small gift, I pray that I might grow further in love for her, and by growing in love for her, I might grow in love for her Son, who gives order to the universe and reason to human beings. Any element of truth or success contained herein is directly attributable to the constant and unfailing help provided for me by Him; every error and untruth contained herein is directly attributable to my own inane pride and sloth which have prevented me from accepting His guidance.

Nathan C. Loyd

Table of Contents

List of Figures

Page

List of Tables

Page

List of Selected Abbreviations and Symbols

Abbreviation/Symbol	Description
a	Electron Attenuation Rate (cm^{-1})
ASTM	American Society for Testing and Materials
BPI	Beam Purity Indicator
CASINO	Carlo Simulation of Electrons in Solids
CSDA	Continuous Slowing Down Approximation
D	Film Density
ICRU	International Commission on Radiological Units
K	Empirical Constant for Electron Range
ℓ	Angular Momentum of Nucleon
L	Angular Momentum Change During De-Excitation
n	Electron Shell Designation or Empirical Constant for Electron Range
NIF	National Ignition Facility
PTFE	Polytetrafluoroethylene
TLD	Thermoluminescent Dosimeter
α	Conversion Coefficient (Conversion Electrons per Gamma)
γ	Conversion Efficiency (Secondary Radiation per Neutron Absorption)
δ	Converter Thickness (cm)
λ	Branching Ratio
λ_n	Neutron Wavelength
ξ	Neutron Lethargy

PASSIVE, LOW COST NEUTRON DETECTORS FOR NEUTRON DIAGNOSTICS AT THE NATIONAL IGNITION FACILITY

I. Introduction

1.1 NIF Collaboration and Problem Identification

The National Ignition Facility (NIF) at the Lawrence Livermore National Laboratory is a multibillion dollar nuclear physics research facility. The facility uses 192 terawatt class lasers to compress a pellet of deuterium. The pellet collapses under pressures and temperatures similar to those observed in stars and nuclear weapons, all in a billionth of a second. Under these forces, the deuterium fuses, resulting in an enormous fluence of neutrons which ricochet throughout the facility and are moderated and absorbed by a 2 m thick concrete wall. Within the target chamber where the fusion occurs, the neutron fluence can reach over 10^{21} neutrons per square centimeter. [1]

NIF researchers are concerned about neutron effects on measurement electronics. Immediately after a shot, the facility is engulfed in a sea of moderated thermal neutrons.

Unmoderated fast neutrons can also travel directly from the fusion event and pass through shield penetrations designed for cables and measurements. The NIF researchers have produced detailed Monte Carlo models of neutron fluences; however, these models have not been fully validated against measurements. In order to make accurate predictions of electronics survivability, the NIF team requires experimentally validated models. [2]

A test plan was developed to perform the necessary measurements. A few critical design constraints were identified. First, access to power supplies and physical space inside the facility is problematic. Because these measurements would be performed by non-NIF personnel, they could be displaced on short notice by a NIF-directed requirement. Therefore, only passive, nonelectrical measurement techniques were considered feasible. Additionally, the facility is highly radioactive immediately after a NIF pulse due to activated construction materials. This causes the facility to be shut down to workers for up to 15 hours post-shot. Finally, the method must be inexpensive, easily reproduced, and portable. This allows for many measurements throughout the facility, and with it, a more thorough validation of the NIF team's neutron fluence models.

A survey of traditional measurement techniques was conducted to identify a method fulfilling the requirements mentioned above. Methods requiring arrays of pulse shaping electronics and power sources were eliminated due to high cost and the necessity of a passive measurement technique. This included fission chambers, self powered detectors, scintillators, and proportional detectors. Bonner spheres are self-contained detectors, but retrieving fluence data from the available analog detectors would be

problematic. Foil activation was also considered. Foil activation is an entirely passive, cheap, and easily reproducible measurement technique. However, because the facility is inaccessible for a long time after a shot, a significant fraction of any induced activity in the foils would decay before samples could be retrieved, transported, and counted. This loss of data was unacceptable. Bubble detectors and Cherenkov detectors were rejected because NIF personnel had already attempted the measurement with these devices, but were unable to draw satisfactory data. Finally, track-etch detectors were considered unfeasible because they required a large investment in automated track counting equipment.

Thermoluminescent dosimeters (TLDs) remained as a viable option. They are passive, cheap, and do not lose information on the timescales involved. However, it was feared that the link between TLD reported dosage and neutron fluence may be tenuous. If a fast neutron produced a higher dose in the TLD crystal than a slow neutron, the interaction of many slow neutrons may be indistinguishable from a few fast neutrons. Therefore, a system that was sensitive to only fast or thermal neutrons was preferable.

A new technique fitting these constrictions was found in the field of neutron radiography. In neutron radiography, neutrons are absorbed by a material known as a converter which subsequently produces ionizing radiation. This ionizing radiation exposes a film emulsion, and the exposure can be quantified. If the film exposure can be directly linked to neutron fluence, reliable measurements could be performed. This method is passive, and depending on the converter material, the device could be cheap and sensitive to only neutrons of a certain energy.

1.2 Statement of Short and Long Term Research Goals

NIF researchers desired a quantification of the number of fast neutrons that penetrated the shield and could damage measurement electronics. In the areas of interest outside of the bioshield, the researchers expect a fast neutron fluence of approximately 1000 neutrons per square centimeter. Unfortunately, the most efficient converter materials typically used in neutron radiography are sensitive to thermal neutrons, and materials sensitive to fast neutrons are not as efficient. A method using alternating layers of neutron moderators and detectors was proposed which could perform fast neutron spectrometry using thermal neutron detectors. At the desired measurement locations, the NIF researchers expect a nearly five to one ratio of thermal to fast neutrons, making a significant source of background radiation to which the detectors would be sensitive. A device known as a Beam Purity Indicator (BPI) was incorporated into the detector concept to distinguish between these thermal neutrons and the fast neutrons directly from the source.

The scope of the project thus grew too large for a single thesis. It was decided to partition the work. Three phases were envisioned:

1. **Develop the neutron radiography technique into a viable thermal neutron detection method.** The proposal to use a thermal neutron converter material coupled with x-ray film is not suitable for fast neutron detection. However, it does have certain attributes, such as ruggedness, passivity, price, and efficiency which are desirable in a thermal neutron detector.
2. **Utilize the thermal neutron detection method to create a neutron spectrometer.** If the thermal neutron measurement technique examined here

proved viable, a fast neutron spectrometer could be constructed using the method described by Bickley et. al. [3]

3. **Perform measurements at the NIF.** A survey of the NIF building could be performed using the spectrometer. As it will be relatively cheap to produce, many spectrometers would be spread throughout the facility, giving a statistically significant data set for model validation.

This work focused on the first phase of the research. Thermal neutron detectors were constructed using x-ray film and gadolinium oxide. The response of the film, measured by film darkness after development, was correlated to known thermal neutron fluences. This data was used to create a simple calibration curve which can be used to relate the measured darkness of the film to an unknown neutron fluence. Based on the programmatic and technical requirements, four success criteria were identified: 1) thermal neutron fluence produces a quantifiable change in the film darkness, 2) the film response is reproducible between separate measurements at equal fluence, 3) the minimum detectable fluence is less than 1000 neutrons per square centimeter, and 4) the error in film darkness measurements correspond to a fluence uncertainty of less than ± 10%. This method failed to meet the last three objectives; therefore, the next phase of the project is not recommended.

II. Theory

2.1 Neutron Radiography

Neutron radiography emerged shortly after the discovery of the neutron in 1932. German researchers, intrigued by the penetrating capability of the neutron, first used neutron beams to image the interior of objects in 1935. [4] Since then, the field has been standardized by ASTM guidelines, and experts hold routine international conferences. Due to the difficulty of obtaining portable neutron sources, neutron radiography has remained relatively small compared to x-ray radiography and is reserved for unique applications.

This research is not directly focused on neutron radiography. Neutron radiography is used for the nondestructive testing of manufactured pieces to examine hidden internal structures visibly. However, the process of producing a neutron radiograph, and the underlying physics thereof, form the basis of neutron detection using x-ray films and gadolinium oxide. This detection mechanism cannot be understood without first examining the science of neutron radiography.

2.1.1 Introduction

Essentially, neutron radiography is the imaging of neutron attenuation in an object. Similar to x-ray radiography, a beam of neutrons is directed through the imaged object and onto a film. The neutrons scatter and are absorbed within the imaged object. After they exit, they are converted into ionizing radiation by a converter material. This

ionizing radiation is then absorbed by x-ray film, producing an image indicative of the scattering and absorption within the object. The end result is a change in the film density (a measure of film darkness) proportional to the localized neutron fluence. Figure 1 illustrates the process.

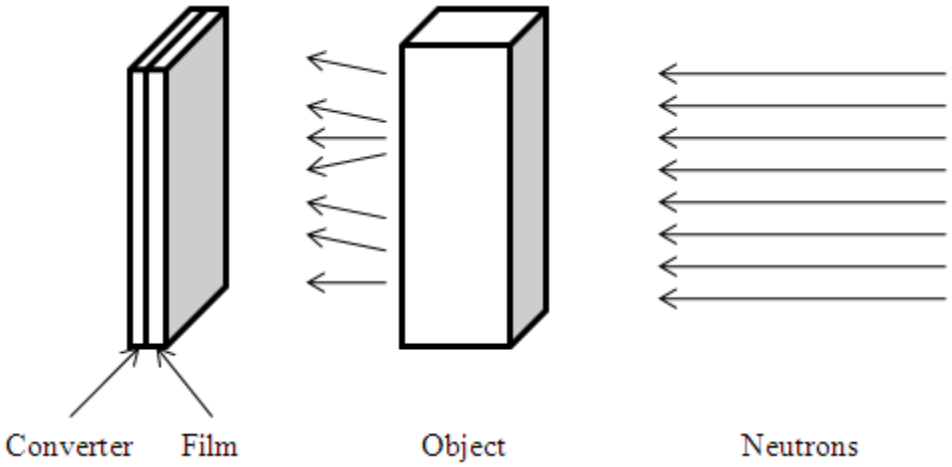

Figure 1 – Schematic of typical neutron radiography. [4]

Neutrons pass through the object, and are attenuated according to the object's isotopic composition and density. This results in patterns of greater film exposure in the regions of lesser attenuation, and lesser film exposure in regions of greater attenuation. Because elements of similar atomic number can have very different attenuation coefficients, differing by more than two decades, neutron radiographs can distinguish features that x-rays cannot. [4] As an example, the large difference in thermal neutron mass attenuation coefficients of uranium and plutonium can be exploited to identify respective regions in a fuel pellet. Conversely, in an x-ray radiograph, both elements would similarly attenuate the penetrating radiation and appear identical in the developed

image. Neutron radiography is commonly used for testing nuclear fuel rods, aerospace components, and ordnance.

Film is very thin compared to the mean free path of neutrons used in imaging. When neutrons do interact within the film, they are unlikely to produce a secondary charged particle which can lead to an image. Therefore, it is preferable that a converter outside of the film first absorb neutrons and then emit some type of ionizing radiation to interact in the film. Converters are made of materials with high neutron absorption cross sections and produce prompt or delayed secondary radiation. Converters are often foils made of gadolinium, indium, dysprosium, or gold. [4]

If the converter produces prompt secondary radiation, the film must be exposed with the converter and the object to be studied. This process is known as direct neutron radiography. This method is sensitive to background gamma radiation. If the secondary radiation comes from activated atoms within the converter which later decay, the converter can be exposed separately from the film, preventing film exposure due to background. The converter is then transferred to the film and allowed to decay, producing radiation which exposes the film and produces an image. This process is called transfer neutron radiography. [5]

Two types of films can be used in neutron radiography. The first and most common is x-ray film, to be described later. Alternatively, nitrocellulose film can be used. While x-ray film produces an image by a photochemical reaction, nitrocellulose films are etched by heavy charged particles. For this reason, nitrocellulose film requires a lithium or boron converter when used with thermal neutrons. When the film is used for fast neutrons, recoil protons are produced by neutron interactions with the hydrogen in

the film. These recoil protons produce etches, and so a converter is unnecessary. In both cases, the microscopic etches are magnified by acid erosion and counted. The density of the tracks corresponds to the neutron fluence. This film has the advantage of being insensitive to background gamma radiation, but is extremely flammable and difficult to handle. [4]

Thermal neutrons are most commonly used in neutron radiography. This is because interaction cross sections for thermal neutrons are nearly always greater than cross sections for fast neutrons and lead to sharper images. It has been observed that exposures on the order of 10^9 neutrons/cm^2 generally produce images with acceptable contrast. [4]

2.1.2 Converters

In general, good converter materials have a high neutron absorption cross section, produce large quantities of ionizing radiation which efficiently expose the film, and are easy to handle. In this research, cost was also a factor. Converter thickness and placement with respect to the film can also impact the efficiency of neutron detection.

The most common converter material is gadolinium. Gadolinium-155 and 157 have the highest absorption cross sections of any stable isotopes, and are relatively abundant in natural gadolinium. After absorbing a thermal neutron, these isotopes produce conversion electrons with energies well suited for exposing film. Further discussion of gadolinium will be provided in Section 2.3.

The versatility of dimensions, specifically thickness, can be exploited to increase the efficiency of the system for neutron detection. According to [5], "The quantity of

radiation issuing from the [converter] must increase and then because of screening and self absorption will tend to attain a constant value for a rear screen and decrease for a front screen." Incidentally, this fact can be used to make the converter-film combination sensitive only to neutrons from a certain direction. The relations shown in equations (2.1) to (2.12), motivated by [5] and [6] but derived by this author, illustrate the link between thickness, efficiency, and directionality.

Figure 2 shows a schematic of the two possible converter configurations. The rear converter configuration will be considered first, and only in the case of direct (that is, prompt) neutron radiography. Furthermore, a gadolinium-based converter will be assumed, but the final conclusions apply to all converter materials emitting prompt secondary radiation.

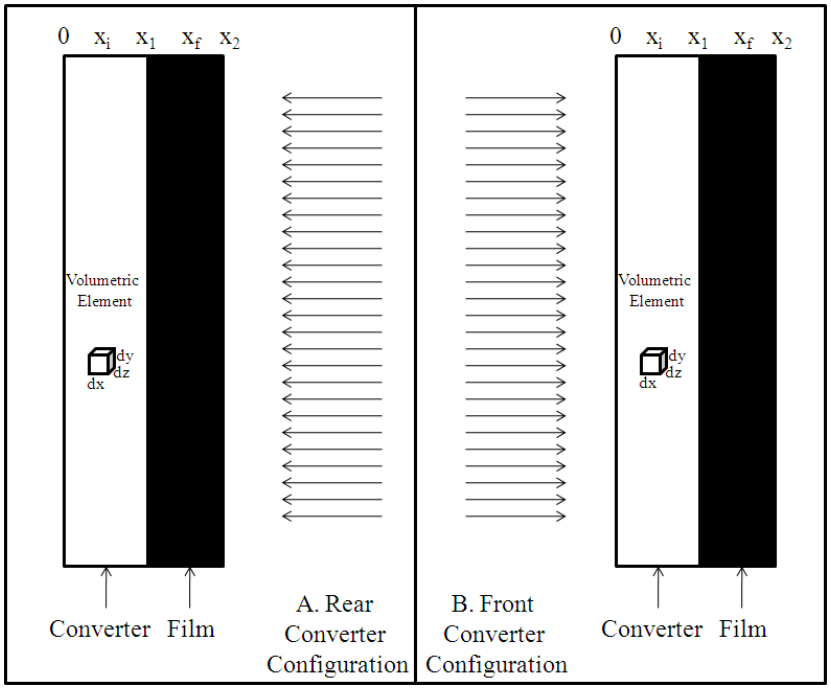

Figure 2 – Illustration of a rear and front converter configuration.

In both figures, a differential volumetric element is shown. The differential reaction rate, dR, is (ignoring neutron interactions within the film)

$$dR = \phi(x_i)\Sigma\, dx\, dy\, dz \tag{2.1}$$

where $\phi(x_i)$ is the neutron flux in neutrons/cm^2·s at location x_i, Σ is the macroscopic cross section of the converter in cm^{-1}, and dx, dy, and dz are the differential element dimensions as shown in Figure 2. Accounting for exponential attenuation of the neutron flux through the converter yields

$$dR = \phi_0 e^{-\Sigma(x_1 - x_i)}\, \Sigma dx\, dy\, dz \tag{2.2}$$

Here, ϕ_0 is the incident flux, x_1 is the converter thickness, and the rest of the symbols are the same as in (2.1). To simplify the derivation, a one dimensional system (left/right movement only) will be used. With this simplification, the total number of absorptions within the converter is

$$R_t = \int_0^{x_1} \phi_0 e^{-\Sigma(x_1 - x_i)} \Sigma dx_i \tag{2.3}$$

In (2.3), dx_i is the differential depth into the converter. The total number of electrons produced, $N_{e,t}$, is therefore

$$N_{e,t} = \gamma \int_0^{x_1} \phi_0 e^{-\Sigma(x_1 - x_i)} \Sigma dx_i \tag{2.4}$$

where γ is the conversion efficiency of the converter material for a given radiation type. For gadolinium, it is the number of conversion electrons per neutron absorption.

Now, radiation losses must be considered. There are two loss mechanisms. First, assuming isotopic radiation, the conversion electrons or gamma rays produced by neutron absorption are equally likely to travel left or right. In a one-dimensional model, half of

the quanta will be directed away from the film. Next, the radiation will be attenuated while traveling to the converter/film boundary. According to Harms [6], electron attenuation is best modeled by an exponential loss, with a known attenuation rate, a, for the given material (see Section 2.4). It will be assumed, as per [7], that the x-ray film is thick enough to register all of the incident radiation. Therefore, the number of electrons generated in the converter and entering (and later exposing) the film is given by

$$\begin{aligned} N_e &= \underbrace{\frac{1}{2}}_{\substack{\text{half travel} \\ \text{rightward}}} \gamma \int_0^{x_1} \phi_0 e^{-\Sigma(x_1 - x_i)} \Sigma \underbrace{e^{-a(x_1 - x_i)}}_{\text{e-'s lost in converter}} dx_i \\ &= \frac{1}{2} \gamma \phi_0 \Sigma \int_0^{x_1} e^{-(\Sigma + a)(x_1 - x_i)} dx_i \end{aligned} \tag{2.5}$$

Letting δ represent the converter thickness and integrating yields

$$N_e = \underbrace{\frac{1}{2} \gamma \phi_0 \Sigma \frac{1}{(\Sigma + a)}}_{\substack{\text{properties independent of} \\ \text{converter thickness}}} \left(1 - e^{-(\Sigma + a)\delta}\right) \tag{2.6}$$

Finally, assuming a constant converter material and fluence,

$$N_e \propto \left(1 - e^{-(\Sigma + a)\delta}\right) \tag{2.7}$$

Equation (2.7) shows that the number of electrons entering the film increases asymptotically, and is maximized for an infinitely thick converter, all else being equal. Therefore, "for a rear screen converter, the secondary radiation flux at the film, independent of the material of the screen and the energy of secondary radiation, increase with increasing thickness and attain maximum values as thickness goes to infinity." [5]

However, this is not true for a front converter. Beginning as with Equation (2.1),

$$dR = \phi_0 e^{-\Sigma(x_i)} \Sigma \, dx \, dy \, dz \tag{2.8}$$

Note that the attenuation is over x_i, not $(x_1 - x_i)$ as before. This is due to the differing geometry, as shown in Figure 2. Assuming a one dimensional steady state,

$$R_t = \int_0^{x_1} \phi_0 e^{-\Sigma(x_i)} \Sigma dx_i \tag{2.9}$$

The number of electrons arriving at the film boundary after isotropic emission and attenuation in the converter is

$$N_e = \frac{1}{2} \gamma \phi_0 \Sigma \int_0^{x_1} e^{-\Sigma(x_i)} e^{-a(x_1 - x_i)} dx_i \tag{2.10}$$

After simplifying and integrating, and with δ representing the converter thickness

$$N_e = \frac{1}{2} \gamma \phi_0 \Sigma \left(\frac{e^{-a\delta} - e^{-\Sigma\delta}}{\Sigma - a} \right) \tag{2.11}$$

If the terms with no dependence on thickness are held constant,

$$N_e \propto \left(e^{-a\delta} - e^{-\Sigma\delta} \right) \tag{2.12}$$

These results are summarized below in Table 1. Tyufyakov [5] and Harms [6] both provide corroborating experimental results for a variety of converter material, thickness, and film combinations. As a corollary to these results, if the thickness is quite large compared to the mean free path of the neutrons and secondary radiation, the film will only be exposed by neutrons traveling from the source. Backscattered neutrons will be absorbed a short distance into the rear of the converter, and associated secondary radiation will not reach the film. This allows directional discrimination. Furthermore, optimal efficiency for a front converter configuration is very difficult to achieve, as the maximum efficiency is typically on the order of 15 μm and quickly decreases. [5] A rear converter, however, has an optimal efficiency at infinite thickness. Maximum efficiency

for gadolinium foil converters is practically achieved near 25 μm, with increased thickness neither increasing nor decreasing the efficiency. [6] As a result, if the converter is a rear converter, efficiency can be maximized easily and, after a very small threshold value, is relatively insensitive to variations in thickness. This is contrasted to a front converter, which is very difficult to optimize, and any error in thickness leads to enormous loss of efficiency. These results will be important for the detector design, to be discussed in Section 3.1.

Table 1 – Converter Performance Characteristics

	Rear Converter	Front Converter
Dependence of Efficiency on Thickness	$N_e \propto \left(1-e^{-(\Sigma+a)\delta}\right)$	$N_e \propto \left(e^{-a\delta}-e^{-\Sigma\delta}\right)$
Maximum Efficiency	$\left(\Sigma+a\right)e^{-(\Sigma+a)\delta}=0$ $\delta=\infty$	$\Sigma e^{-\Sigma\delta}-ae^{-a\delta}=0$ $\delta=\frac{\ln\left(\frac{a}{\Sigma}\right)}{a-\Sigma}$
Limit as Thickness Increases	$\lim_{\delta\to\infty}\left(1-e^{-(\Sigma+a)\delta}\right)=1$	$\lim_{\delta\to\infty}\left(e^{-a\delta}-e^{-\Sigma\delta}\right)=0$

2.1.3 Beam Purity Indicators

X-ray film is sensitive to the gamma rays that are concomitant with nearly all nuclear processes producing neutrons. Gamma background radiation is nominally required to be limited to one photon per three neutrons. If this ratio is maintained, roughly 90% of the film darkening should be due to neutrons, and 10% due to photons. [8] However, film only has one mechanism of response to the radiation, and that is to become darker. This makes parsing neutron exposure from gamma exposure difficult. One cannot immediately identify if a region of film exposed with a converter was

exposed by gamma rays, scattered neutrons, or direct neutrons. This can be problematic for neutron radiography, as gamma rays are attenuated much differently than neutrons. If a high gamma exposure component is not identified, a neutron radiograph may inaccurately indicate areas of low neutron attenuation. ASTM has developed a standard test item, known as a Beam Purity Indicator (BPI), to be irradiated with the converter-film assembly to quantify the contribution from each type of radiation. [9],[10]

The BPI is a 1 inch × 1 inch × 0.25 inch block of polytetrafluoroethylene (PTFE) embedded with two disks of lead and two disks of boron nitride, as shown in Figure 3. A large hole is drilled through the center of the block. One disk of lead and one disk of boron nitride are pressed into holes drilled near two corners on a block face. The process is repeated on the opposite face, flipped so that no disk is shielded by another, and one set of disks will lie near the film surface. Cadmium bars are place on either face of the block between the disks. However, these are used to qualitatively analyze the collimation ratio, a factor important in image resolution. Since image resolution is not important to this research, the cadmium bars were excluded.

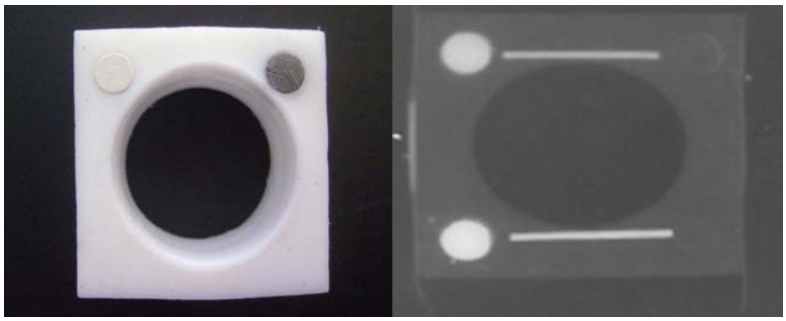

Figure 3 – A photograph and neutron radiograph of a BPI. [11] The orientation of the BPI is identical in each. The neutron radiograph shows two bright lines where cadmium bars are typically placed.

According to the designer of the BPI [12], the materials and dimensions of the device were specifically chosen for their attenuation characteristics of gamma rays and neutrons. PTFE and lead are nearly transparent to thermal neutrons, but the lead blocks most gamma rays. Similarly, PTFE and boron are transparent to gamma rays, but boron blocks almost all thermal neutrons. Placing two lead disks in the device allows for a comparison between high and low energy gamma content. Both lead disks block low energy gamma rays, and many high energy gamma rays. High energy gammas are likely to cause pair production in the lead. The lead disk far from the film will produce 511 keV pair production gammas that radially disperse and do not expose the film, but the lead disk nearest the film will produce the same gamma rays sufficiently near the film to cause exposure. Comparison of the two regions gives an indication of the high energy gamma content of the beam, while the difference between the lead disks and the PTFE shadows indicate the exposure due to low energy gamma radiation.

Determination of the direct and scattered neutron contributions is based on the images of the boron disks. The disk closest to the film prevents both scattered and direct neutrons affecting the film. The disk far away from the film surface blocks direct neutrons, but allows scattered neutrons (that is, neutrons that are not normal to the plane of the converter) to reach the converter layer. These two exposures give an indication of the contribution from each neutron source. [12]

Quantitative analysis is performed by film density measurements (see Section 2.5.3), with the knowledge that film density is linear with the logarithm of radiation fluence. No synergistic effects have been observed between these radiation types. [7] Table 2 gives the ASTM equations for determining each contribution.

Table 2 – ASTM Equations for Radiation Contributions to Film Exposure

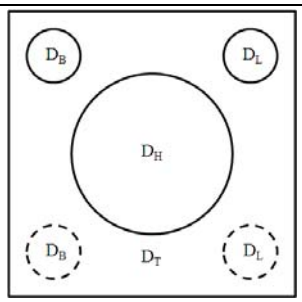 D_H, D_B, D_L, and D_T are the film density behind the hole, boron disks, lead disks, and PTFE.	Direct Thermal Neutron Content	$\frac{D_H - (higher\ D_B + \Delta D_L)}{D_H} \times 100$
	Scattered Neutron Content	$\frac{\Delta D_B}{D_H} \times 100$
	Low Energy Gamma Content	$\frac{D_T - lower\ D_L}{D_H} \times 100$
	High Energy Gamma Content	$\frac{\Delta D_L}{D_H} \times 100$

2.2 Neutrons

Neutrons are elementary particles of an atomic nucleus. They have a mass of 1.00866501 atomic mass units, and no charge. Neutrons are unstable outside of the confines of the strong nuclear force. Consequently, free neutrons β- decay into free protons with a half-life of 10.6 minutes. [13]

Because free neutrons are unstable, they can only be obtained by removal from a nucleus. This is accomplished by exciting a nucleus with enough energy to overcome the binding energy securing the neutron. [5] A specific reaction leading to the production of free neutrons will be presented in Section 2.2.2.

Neutron energies are, for nonrelativistic velocities, given as

$$E = \tfrac{1}{2} m_n v^2 \qquad (2.13)$$

According to quantum mechanics, the neutron, as any other elementary particle, behaves as both a wave and a particle. The wavelength of a neutron is determined by the de Broglie formula:

$$\lambda_n = \frac{h}{m_n v_n} \tag{2.14}$$

where h is Planck's constant, 4.13570×10^{-15} eV·s, and λ_n is expressed in meters. After substituting the kinetic energy of the neutron and the value of Planck's constant, the wavelength as a function of energy is

$$\lambda_n = \frac{2.86\times10^{-11}}{\sqrt{E_n}} \tag{2.15}$$

Here, E_n is in eV, and λ_n is in meters. [5]

Neutrons are conventionally categorized according to energy and typical interactions with matter. Table 3 presents four common neutron classifications. For comparison to these wavelengths, the Bohr radius is 5.29×10^{-11} m. [13] Low energy neutrons, then, can potentially interact with multiple nuclei in a compound simultaneously.

Table 3 – Neutron Energy Groups

	Energy	Wavelength from Eq (2.15), m
Cold	$< 5\times10^{-3}$ eV	4.0×10^{-10}
Thermal	0.025 eV	1.8×10^{-10}
Epithermal	~ 1 keV	9.0×10^{-13}
Fast	100 keV – 10 MeV	$9.0\times10^{-14} – 9.0\times10^{-15}$

2.2.1 Interaction with Matter

Neutrons are only affected by the strong nuclear force. Therefore, interactions with neutrons occur on the range of the strong nuclear force, or about 10^{-15} m. Because the wavelength of a neutron changes with its energy, the type of interaction with a stationary nucleus also varies. High energy neutrons have shorter wavelengths, and behave more akin to a particle than a wave. As a result, high energy neutrons are likely to collide with the surface of a nucleus. Low energy neutrons have wavelengths commensurate with a nuclear radius. As such, they can penetrate the surface of the nucleus and are far more likely to be absorbed. [5]

In a collision, the incident neutron transfers a portion of its energy to the target nucleus. The defining characteristic of this interaction is that the neutron remains free. In an elastic collision, total kinetic energy is conserved. Inelastic collisions result in the conversion of kinetic energy to excitation energy in the impacted nucleus. The incident neutron must possess a threshold amount of energy to excite a nucleus. The requisite energy varies depending on the mass and nuclear structure of the target, but in general, heavy nuclei require hundreds of keVs, while light nuclei require MeVs. If a neutron does not have the threshold amount of energy, elastic collisions become more likely. [5] The energy lost by a neutron can be determined using classical mechanics and assuming point particles:

$$E_{n2} = E_{n1} \frac{M_R^2 + 2M_R m_n \cos\theta + m_n^2}{\left(M_R + m_n\right)^2} \tag{2.16}$$

M_R is the mass of the nucleus, m_n is the mass of the neutron, θ is the deflection angle, and E is the energy. The maximum energy is lost when $\theta = \pi$, and greater energy losses are

observed in collisions with low mass nuclei. Scattering is therefore used to remove energy from fast neutrons and create thermal neutrons.

If a neutron's wave function interacts sufficiently with that of a nucleus, the neutron is absorbed. Very often, this absorption leads to an excited reaction product, which then de-excites by emitting secondary radiation quanta or fissioning. The type, energy, and frequency per absorption of this secondary radiation are highly dependent on the incident neutron energy and the structure of the nucleons in the nucleus. If the reaction is described as

$$A + n \rightarrow B + x \tag{2.17}$$

then the energy of the reaction, called the Q-value, is calculated by

$$Q = \left[\left(M_a + m_n \right) - \left(M_b + m_x \right) \right] c^2 \tag{2.18}$$

Equation (2.18) is the conservation of energy of the reaction, and reflects the mass-energy equivalence, $E = mc^2$. [13] The Q-value can be less than zero, indicating an endothermic reaction requiring a threshold neutron energy, or exothermic, indicating a spontaneous reaction with any neutron energy. [5]

Besides energy, other quantities are conserved in a reaction. On the time scale of nuclear reactions (10^{-16} s), the weak force can be neglected, and therefore proton and neutron number are conserved. The angular momentum and parity, that is, spin states of nuclei and nucleons, are also conserved. [13] This is an important consideration that helps to determine the state of any intermediary composite nucleus, and with it, type, energy, and frequency of emitted radiation. Details of the spin correlation to emitted radiation will be illustrated using gadolinium neutron absorption as an example in

Section 2.3. For now, it is expedient to describe the conservation of angular momentum and parity. The nuclear spin, I_f, of a capturing state is determined by the orbital angular momentum ℓ and the spin angular momentum s of the incident or emitted particle added to the nuclear spin, $I_{i,target}$:

$$I_f = I_{i,target} + \ell + s \tag{2.19}$$

and the parity is conserved as:

$$\pi_f = \pi_{i,target}(-1)^{\ell} \tag{2.20}$$

where $\pi_{i,target}$ is the initial parity, π_f is the final parity, and ℓ is the orbital angular momentum. According to the laws of quantum mechanics, thermal neutron capture restricts I_f to $I_i \pm 1/2$, and $\pi_f = \pi_i$. [13]

The probability of any interaction, either collision or absorption, is expressed by the reaction cross section, σ.

$$R = \sigma \frac{\rho N_a}{A} \phi = \Sigma \phi \tag{2.21}$$

where R is the number of reactions per unit time and volume, σ is in units of area, ρ is the material density, N_a is Avogadro's number, A is the atomic mass of the material, and ϕ is the neutron flux in neutrons/cm^2·s. [13] Σ, called the macroscopic cross section, takes into account gross material properties, and has units of inverse length. Essentially, σ is a measure of the number of reactions for a single nucleus per incident neutron. When this quantity is multiplied by the number of atoms in a volume and the neutron fluence, the total number of reactions in a volume is obtained. While the cross section can be determined from theoretical principles, calculated results do not always correspond to experimental values.

The total cross section is merely the sum of partial cross sections for each type of reaction. It is typically measured in units of barns, where 1 b = 10^{-24} cm^2. If a material is a compound, rather than a pure element, the weighted sum of the cross sections is taken to give the total material cross section. This is a mostly accurate method; however, slow neutrons have wavelengths that are long enough to penetrate two adjacent nuclei in some compounds, leading to correction factors that are molecule dependent. [5] This effect is minimal, and will be ignored for this work.

2.2.2 Sources of Neutrons

As mentioned previously, free neutrons can only come from interactions which excite bound neutrons and remove them from a target nucleus. There are four primary methods to accomplish this. The first is to induce fission in a heavy nucleus, which causes fission fragments and, in the process, free neutrons. The second is from fusion of light nuclei. Next, charged particles, especially alpha particles, can cause the ejection of a neutron upon collision with a nucleus. Finally, if a very high energy gamma ray collides with the nucleus, its energy can cause nuclear excitation and the emission of a neutron. In this research, an alpha reaction will be used; specifically, the AFIT plutonium beryllium graphite moderated source.

The reaction initiated by an alpha particle and resulting in a free neutron can be considered as (assuming initial kinetic energies are negligible)

$$ {}^{A}_{Z}A + {}^{4}_{2}\alpha \rightarrow {}^{A+3}_{Z+2}B + n + Q \tag{2.22} $$

These reactions can be endothermic or exothermic, depending on the target A. Because alpha particles are massive and charged, they must have enough energy to penetrate the

Coulomb barrier of the nucleus. The reaction cross section accordingly increases with alpha energy. A low-Z target, thus having lower nuclear charge, also increases the reaction cross section. Common targets therefore are lithium, boron, and beryllium. Of these, beryllium has the highest reaction Q-value of 5.7 MeV. [5]

Alpha particles lose energy quickly as they travel through a material, and particles from a monoenergetic alpha source will have a distribution of energies upon reaching target nuclei. Complicating the matter is the impossibility of making a completely homogenous alpha source and target mixture, causing alphas to travel different distances before interacting. [14] Therefore, the neutrons emitted from an (α,n) reaction will also have an energy distribution, as shown for a plutonium beryllium source below.

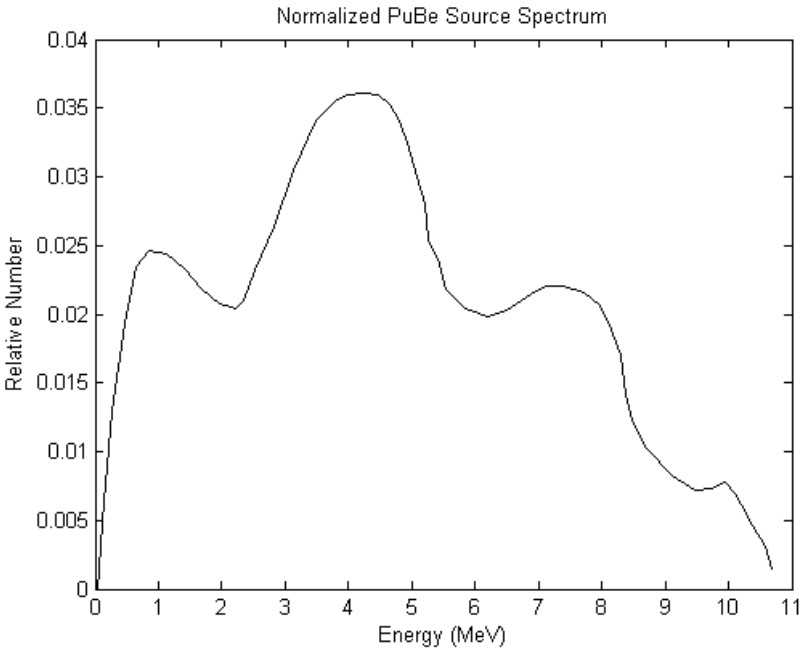

Figure 4 – A PuBe source neutron energy spectrum. [15]

Neutrons are freed with large amounts of energy, reflective of the large Q-values of the reactions and kinetic energy of the alpha particles. Obtaining a thermal neutron flux requires moderation of these fast neutrons by elastic scattering within a material. The maximum energy loss of a neutron during an elastic collision is given by analysis of (2.16). Neutron lethargy, ξ shown below, has been introduced to express the average energy loss per collision: [16]

$$\xi = 1 + \frac{(A-1)^2}{2A} \ln \frac{A-1}{A+1} = \frac{1}{n} \ln \frac{E_i}{E_f} \tag{2.23}$$

In (2.23), A is the mass of the target, n is the number of collisions, and E is the initial and final neutron energy. It can be concluded that neutron lethargy is inversely related to the number of collisions necessary for a given energy decrement.

Increasing probability of elastic scattering, expressed by Σ_s, decreases the volume of material necessary for a given energy loss. Therefore, materials with high values of $\xi\Sigma_s$ are better moderators. Another consideration is that as neutron velocity decreases, the probability of absorption by a moderating nucleus rather than scattering increases. Materials with low macroscopic coefficients for absorption are optimal. The best moderating materials are those that have a high $\xi\Sigma_s/\Sigma_a$. For comparison, heavy water has a ratio of 5670, while graphite is 192, and lead is 0.62. [5]

Completely moderated neutrons are in thermal equilibrium with the moderating material. The neutron field can be modeled as a gas, and has a Maxwellian energy distribution based on the temperature of the moderating material:

$$f(E)dE = 2\pi n \left(\frac{1}{\pi kT} \right)^{3/2} E^{1/2} e^{-E/kT} dE \tag{2.24}$$

In (2.24), n is the total number of neutrons, k is the Boltzman constant, T is temperature, E is energy, and $f(E)$ is the fraction of neutrons with energies between E and $E+dE$. [13] This is an approximation, however; the actual temperature of the neutrons is, in general, ten degrees higher than the moderator due to leakage from the moderator surface and absorption within the moderator. [5]

2.2.3 AFIT Graphite Moderated Plutonium Beryllium Source

The AFIT thermal neutron source was installed in 1962. The PuBe source is housed in a large graphite moderator with removable stringers, as shown in Figure 5, "enclosed by an attractive aluminum honeycombed insulating panel". [17]

The plutonium in the source alpha decays with various half lives and energies depending on the isotope. Table 4 shows details for each of the long lived plutonium isotopes. The exact isotopic ratios in the plutonium source are unknown. Importantly, Pu-241 decays by beta emission to become Am-241, an alpha emitter. As isotopes of Pu-241 decay and Am-241 quantities increase, additional alpha particles are produced by Am-241 atoms, resulting in an increase in overall neutron flux. The growth of Am-241 has become a factor over the time since installation due to the 14 year half life of Pu-241.

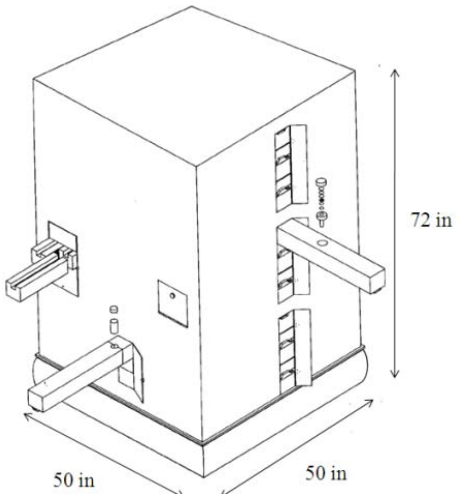

Figure 5 – AFIT graphite pile. [17]

Table 4 – Important Isotopes within a PuBe Source [18]

Isotope	Half Life (Years)	Decay and Q-Value (keV)	Daughter
Pu-238	87.7	α, 5593.2	U-234
Pu-239	2.411×10^{4}	α, 5244.52	U-235
Pu-240	6561	α, 5255.67	U-236
Pu-241	14.325	β-, 20.78	Am-241
Pu-242	3.75×10^{5}	α, 4984.7	U-238
Am-241	432.6	α, 5637.81	Np-237

In 2010, the source was calibrated to correct the 1960 values of neutron production rate and flux within the pile for Am-241 accretion. A 17% gain in the total source strength over the original values was calculated, increasing from approximately 8.63×10^{6} neutrons/s to 1.01×10^{7}. [19] Using foil activation techniques, the thermal neutron flux was determined at the locations of removable stringers. Table 5 presents the experimental fluxes and corresponding uncertainties reported in [19].

Table 5 – AFIT Thermal Neutron Source Measurements [19]

Position Reference	Approximate Axial Distance from Source (cm)	Experimental Flux (n/cm^2·s)	Uncertainty (±)
2	-5	7945	413
3	12	9028	469
4	32	6778	352
5	55	3699	193
6	75	1728	89
7	95	808	43

2.3 Gadolinium

Gadolinium-155 and 157 have the highest absorption cross sections for thermal neutrons of any stable isotopes, at approximately 60,000 b and 255,000 b, respectively. Even though these specific isotopes form less than a third of the atoms of natural gadolinium, the metal is extraordinarily efficient at absorbing thermal neutrons. Figure 6 illustrates this, with isotopic abundances from [20], and cross section data from [21]. While Gd-155 and 157 have the highest cross sections of gadolinium isotopes, Gd-158 has the highest natural abundance. The cross sections of Gd-155 and 157 are so large that the average over all isotopes is still very near the cross sections of Gd-155.

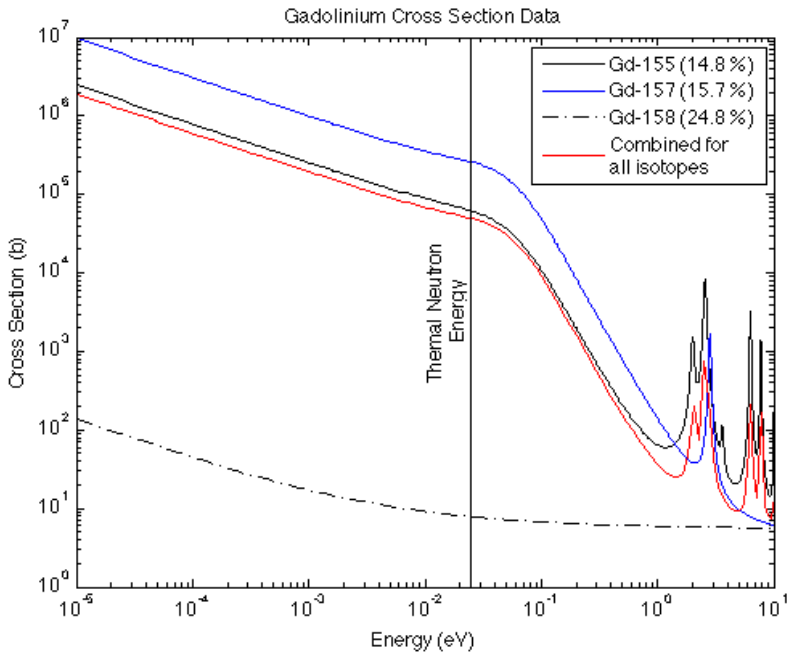

Figure 6 – Cross sections of Gd-155, 157, 158, and total for natural gadolinium as a function of incident neutron energy.

After absorption of a neutron, Gd-155 and 157 frequently emit conversion electrons capable of exposing film. For these reasons, gadolinium is commonly used as an efficient and effective converter for neutron radiography.

2.3.1 Shell Model

The angular momentum, or spin, of a nucleus is given by the sum of the orbital angular momentum, ℓ, and the intrinsic angular momentum, *s*, so that $j = \ell + s$. The orbital angular momentum is determined by different quantum states, or shells, which can hold a certain number of nucleons. Furthermore, the spin of a nucleon is 1/2. Therefore, for a given shell, two values of angular momentum are possible, $\ell \pm 1/2$, depending on the orientation of how the nucleon fills the shell. The ℓ values are indicated by

spectroscopic notation, with $\ell = 0,1,2,3,4,5,6$ corresponding to s, p, d, f, g, h, and i shells, respectively. A g-shell nucleon, for example, can have a spin of 7/2 or 9/2.

Another factor describing the state of a nucleus is nuclear parity. This is indicative of the symmetry of the wave function of the nucleus. If the wave function defining the nucleus is symmetric (similar to an even function such as cos(x)), the nucleus is said to have positive parity; if it is symmetric but negative, (such as sin(x)) there is negative parity. Parity is determined by the shell number as $\pi = (-1)^{\ell}$.

These principles allow determination of the overall spin of a nucleus, and, with it, allowable excitation energies, decay mechanisms, and relative stability. In general (barring some exceptions, primarily for nuclei between 150 and 200 atomic mass units), the shell model predicts that the spin of a nucleus is determined by unpaired nucleons, with protons and neutrons being considered separately. Paired, that is, even numbers, of nucleons are modeled as having opposing, and thus cancelling, spins. This creates a more stable spin state. Spins of an unpaired protons and neutrons are summed as

$$|j_1 - j_2| \le I \le |j_1 + j_2| \tag{2.25}$$

and the overall nuclear parity is given by

$$\pi = (-1)^{\ell_1} (-1)^{\ell_2} \tag{2.26}$$

As mentioned previously, angular momentum and parity of both the target nucleus and incident neutron are conserved during absorption. Thermal neutrons can only be absorbed in a particular wave state, thereby limiting the final angular momentum to $I_f = I_i \pm 1/2$, and $\pi_f = \pi_i$. [13] Table 6 and Table 7 show the quantitative analysis of this reaction in Gd-155 and 157, calculated by (2.18), (2.25), and (2.26). The results

were verified by [22] and [23]. In the tables below, a nominal radiation product is used to indicate that the energy is carried away by either a photon or conversion electron.

Table 6 – Thermal Neutron Absorption in Gd-155

Reaction	^{155}Gd	+	n	→	$^{156}Gd^{*}$	→	^{156}Gd	+	Radiation
Conservation of Angular Momentum and Parity	$3/2^{-}$		± 1/2		1^{-} or 2^{-}		0^{+}		
Conservation of Energy and Mass	154.9226 amu		1.0087 amu		155.9313 amu		155.9221 amu		8.536 MeV

Table 7 – Thermal Neutron Absorption in Gd-157

Reaction	^{157}Gd	+	n	→	$^{158}Gd^{*}$	→	^{158}Gd	+	Radiation
Conservation of Angular Momentum and Parity	$3/2^{-}$		± 1/2		1^{-} or 2^{-}		0^{+}		
Conservation of Energy and Mass	156.8240 amu		1.0087 amu		157.9326 amu		157.9241 amu		7.937 MeV

2.3.2 Spin, Parity, and Nuclear Decay

The precise mechanism of de-excitation for a nucleus is dependent on the change in spin and parity during the transition. Gamma decay and conversion electron emission are both a transition of energy from electric or magnetic multipoles. Multipoles describe the distribution of electric and magnetic fields around the nucleus, and in turn are closely related to nuclear angular momentum. Krane [13] provides the following relation between spin change during de-excitation and contributing multipoles:

$$\left|I_i - I_f\right| \le L \le \left|I_i + I_f\right|$$
$$\Delta\pi = \text{no; even electric, odd magnetic} \qquad (2.27)$$
$$\Delta\pi = \text{yes; odd electric, even magnetic}$$

In (2.27), L is the angular momentum of the transition, such that total angular momentum is conserved by $I_f = L + I_i$. Note that L here is the change in angular momentum, which is different than ℓ used in (2.25) and (2.26) to indicate the angular momentum of a shell. The angular momentum change is also the order of the multipole. For example, a nucleus transitioning from a spin of $3/2^+$ to $5/2^+$ would do so by either an M1, E2, M3, or E4 multipole de-excitation.

The order and type of multipole de-excitation is directly related to the probability of emitting conversion electrons, which are responsible for film exposure in this research. Conversion electrons are bound electrons whose wave functions interact with and gain energy directly from the nucleus. As a result, conversion electron emission competes with gamma emission for decay from a given multipole. If the conversion coefficient, $\alpha = \lambda_e / \lambda_\gamma$ is defined as the ratio of conversion electron and gamma emission decay constants for a certain energy and multipole decay (and therefore the number of emitted conversion electrons to gammas), then the approximate value is given as

$$\alpha(ML) \cong \frac{Z^3}{n^3}\left(\frac{e^2}{4\pi\epsilon_0\hbar c}\right)^4\left(\frac{2m_e c^2}{E}\right)^{L+3/2} \tag{2.28}$$

for a magnetic multipole de-excitation, and

$$\alpha(EL) \cong \frac{Z^3}{n^3}\left(\frac{L}{L+1}\right)\left(\frac{e^2}{4\pi\epsilon_0\hbar c}\right)^4\left(\frac{2m_e c^2}{E}\right)^{L+5/2} \tag{2.29}$$

for an electric de-excitation. In both equations, Z is the number of electrons, n is the shell of the electron emitted (K = 1, L = 2, M = 3, etc.), L is the order of the multipole, E is the energy of the de-excitation, m_e is the mass of an electron, and $\left(e^2/4\pi\epsilon_0\hbar c\right)$ is the fine

structure constant. [13] From these, a few trends can be noted. First, the number of protons in a nucleus greatly affects the probability of a conversion electron emission. The conversion coefficients also increase substantially with an increase in multipole order; however, this is offset by the fact that high order multipoles are much less likely to occur than low order multipoles. Finally, decay mechanisms resulting in large excitation energies tend toward gamma emission, excluding the possibility of conversion electrons carrying energy on the order of MeVs.

It must be noted that the excited nucleus rarely decays to its ground state directly. For instance, post-absorption Gd-156* does not decay directly to Gd-156, and therefore the spin does not change directly from 2^- to 0^+. There are many interstitial nuclear energy levels, with angular momenta greater than 2. [22] Typically, a primary set of high energy gamma rays will be produced that quickly shed a large portion of the excitation energy. This will be followed by lower energy decays removing the remaining energy.

These aspects help explain conversion electron emission from Gd-156 and Gd-158. After an initial set of high energy gamma emissions, both isotopes complete a final set of low energy decays, as shown in Figure 7. Most of these decays occur on the order of picoseconds. [22][23]

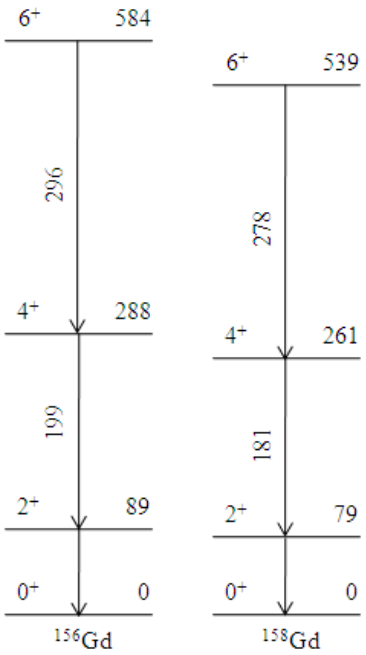

Figure 7 – Low energy decay schemes for Gd-156 and Gd-158. [24] Energies are in keV.

From the rules shown in (2.27), it can be concluded that the transitions shown in Figure 7 are predominantly due to E2 transitions. This is because there is no parity change in the transitions $(\Delta\pi = \text{no})$, and $I_f - I_i = 2$. While the spin change is limited to between 6 - 4 = 2 and 6 + 4 = 10 for the highest level decay, and between 4 - 2 = 2 and 4 + 2 = 6 for the middle decay, low order multipole de-excitations are greater than 1000 times more likely. [13]

Knowledge of the decay schemes, energies, and intensities can be used to determine conversion coefficients for these two isotopes. Harms [24] has coupled this information with cross sections and isotopic abundances to determine conversion electron production rates in natural gadolinium. These values are reproduced in Table 8 below. Note that the energy of a conversion electron is the transition energy minus the electron shell binding energy.

Table 8 – Conversion Electron Production in Natural Gadolinium. [24] Only relatively high intensity transitions (greater than 4 electrons per 100 neutron absorptions) are shown.

Source Isotope	Transition Energy (keV)	Conversion Electron Energy (keV)	Intensity (electrons per 100 neutron captures in natural Gd)
Gd-156	89	39	4.19
Gd-156	89	81	4.97
Gd-158	79	29	9.82
Gd-158	79	71	26.80
Gd-158	79	78	6.17

Overall, for every 100 neutron absorptions in natural gadolinium, 59.91 conversion electrons are produced (including low-intensity transitions not shown above). It can be assumed that when gadolinium is used as a converter material, isotopic emission will result in approximately 30 electrons traveling in the direction of the film. This corresponds to the nominal 30% efficiency reported by [4] for gadolinium conversion screens.

2.4 Electron Transport

Electrons have a charge to mass ratio of 1822 elementary charge units per atomic mass unit. For comparison, a proton has a charge to mass ratio of 0.9928, and the ratio for an alpha particle is 0.4998. [13] As a result, when an electron travels through matter, enormous Coulombic forces are applied to a very small mass, resulting in very large accelerations. Work is performed on the energetic electrons as they traverse the electric fields of constituent atoms, causing a gradual reduction in kinetic energy and the

concomitant release of bremsstrahlung photons and atomic ionization. Energy can also be lost by collisions with bound electrons. The end result of these enormous accelerations and progressive energy losses is a random, involute path, as illustrated in Figure 8.

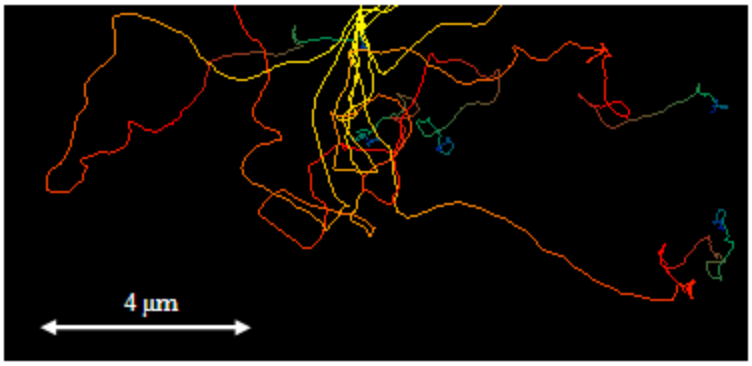

Figure 8 – Example electron tracks generated by the CASINO electron transport program. 100 keV electrons were simulated in a lead slab. The track colors change with energy loss.

The ability of a material to remove energy from an electron is known as the stopping power. The total stopping power is given as a differential rate of energy loss per unit length, and is itself a function of energy. That is, a faster electron loses less energy than a slow electron for every unit of distance traveled. This is because a slow electron is more likely to interact with the material than is a fast electron. [25] The total stopping power of a material is the combination of collisional and radiative stopping power, as show in (2.30).

$$\left(-\frac{dE}{dx}\right)_{tot} = \left(-\frac{dE}{dx}\right)_{col} + \left(-\frac{dE}{dx}\right)_{rad} \tag{2.30}$$

The ratio of collisional stopping power to radiative stopping power is largely a function of electron energy and material atomic number. Generally, the cloud of

electrons surrounding a nucleus shields passing electrons from the nuclear charge. However, high energy electrons are able to penetrate this cloud and interact with the nuclear charge, making radiative losses likely. For heavy atoms, electrons are in general bound more tightly, making collisional losses less efficient. The relationship between these coupled processes is expressed empirically by: [25]

$$\frac{\left(-dE/dx\right)_{rad}}{\left(-dE/dx\right)_{col}} \approx \frac{ZE}{800} \tag{2.31}$$

where Z is the atomic number of the material, and E is the energy of the electron in MeV. Radiative losses are minimal compared to collisional losses for slow (below 1 MeV) electrons.

To generalize the amount of energy needed to remove an electron from an atom, the concept of mean excitation energy, I, has been introduced. It is the energy required to remove an electron from an atom, averaged over all of the atom's shells and associated binding energies. The mean excitation energy for low-Z elements is lower than that of high-Z elements, indicating that electrons in low-Z elements are less forcefully bound. This leads to easier transfer of energy from low energy electrons. As a corollary, the mass collisional stopping power (that is, collisional stopping power divided by material density) generally decreases with increasing Z, indicating that high-Z materials are not efficient at collisional stopping. [26]

While in general, the mean excitation energy of a compound is simply the weighted average of the excitation energy of its components (known as the Bragg additivity rule), a few factors can introduce deviations. First, a density effect has been observed where, all else being equal, stopping power is reduced by density. According to

ICRU Report 37 [26], the passage of charged particles through the medium can polarize the atoms in the medium. This polarization reduces the electromagnetic field, thus reducing the force available to slow the passing electron. The density effect is due primarily to the dielectric response in the material, so that it is more prominent for conductors. For insulators, a threshold electron velocity must be reached before the density effect occurs. A second factor is that the strength of chemical bonds in the compound may increase or decrease the mean excitation energy compared to the simple weighted average of constituent atoms. However, this effect is minimal, and limited to a difference less than ± 2% in most common compounds. The mean excitation energy for elemental media and many compounds can be retrieved from tables such as [26]. For unlisted compounds, the Bragg additivity rule can be employed. If the chemical structure is known (for instance, the presence of carbon in a double or single covalent bond), the excitation energy can be modified for greater fidelity by using the listed excitation energies of specific element-bond combinations. The density effect can be determined, when applicable, by equations presented in [26].

Incidentally, the Bragg additivity rule is also applicable to stopping powers, as shown below:

$$S/\rho = \sum_j w_j \left(S/\rho\right)_j \tag{2.32}$$

Here, ICRU notation has been preserved. S is equivalent to $\left(dE/dx\right)$, and is divided by material density to be density independent. The weight fraction of each element is denoted as w_j. The Bragg additivity rule applies to the collisional, radiative, and total stopping powers of a material.

The range of an electron in matter is approximated using the continuous slowing down approximation (CSDA). In this approximation, the electron energy is assumed to decrement continually along its path, rather than discretely to random interactions. The range is the distance the particle must travel until all of its energy is shed. Notionally, it is represented as

$$R(T) = \int_0^T \left(\frac{-dE}{dx} \right)^{-1} dE \tag{2.33}$$

Where R is the range, T is the kinetic energy, E is energy, and x is distance. Equation (2.33) cannot be evaluated in closed form, as the stopping power is itself a function of energy. CSDA ranges are solved numerically, and listed for many compounds and elements in [26].

Turner [25] provides empirical equations for determining the typical distance an electron will penetrate a low-Z material. For an electron less than 2.5 MeV,

$$R = 0.412 T^{1.27 - 0.0954 \ln T} \tag{2.34}$$

where R is in g/cm^2 and T, the kinetic energy of the electron, in MeV.

Harms [6] and Garside [27] have observed good experimental fidelity using simple exponential attenuation to model electron loss and penetration in a material. These models are based on experimental evidence that the average energy loss per unit thickness remains practically constant throughout the entire penetration depth. [28] Empirically, the range in μm is given by [27] as

$$R = \frac{KE^n}{100\rho} \tag{2.35}$$

where K and n are constants, E is in keV, and ρ is in g/cm^3. According to [28], K is 11.5, and n is 1.35. However, [27] gives K as approximately 10, and n in a range between 1.35 and 1.65.

It must be noted that the values of penetration range and attenuation coefficient are nominal, and given as a guide. For example, given the density of Mylar as 1.39 g/cm^3 [29], the range of a 71 keV electron by (2.34) is 52 μm, 26 μm by (2.35) with K =11.5 and n = 1.35, and 82 μm with K =10 and n = 1.65. The CSDA range provided by [26] is 60 μm. Although it is impossible to analytically determine the attenuation of electrons in matter in the same manner as neutron or photon attenuation, these values can aid in making general conclusions about material performance.

2.5 X-Ray Film

The primary mechanism of modern film-based imagery is a photochemical reaction in silver halide salt grains which converts the silver from crystalline to metallic form. As early as the 1500s, silver halide crystals (notably, crystals of silver bromide) were observed to be particularly sensitive to light. In the 1800s, French scientists used thin layers of silver halide crystals to form primitive photographs. The process has since been studied and perfected, leading to the production of modern films.

2.5.1 Construction

The vast majority of materials in the film are used to physically support and protect the sensitive silver halide crystals. There are typically layers to reinforce the film,

suspend the silver halide crystals, and protect the film surface. [5] These are the base, emulsion, and protective surface layers, respectively, as illustrated in Figure 9.

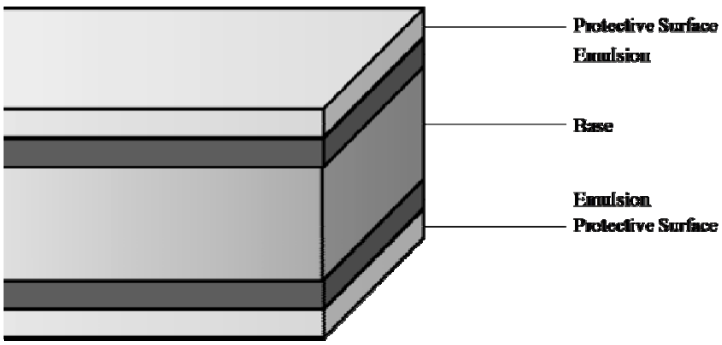

Figure 9 – Cross section of a double emulsion x-ray film. The total film is approximately 0.5 mm thick. Thicknesses are not shown to scale. [30]

The base is often formed from cellulose acetate or polyester. It is transparent to ensure that photons reach both layers of the emulsion, if two layers are present. The base provides a strong skeleton to reinforce the thin emulsion layers. [5]

The emulsion layers contain the silver halide crystals in a gelatin suspension. The gelatin is an organic substance produced by purifying collagen from animals. It provides a sturdy matrix to uniformly distribute the silver halide crystals, while also being permeable to developing chemicals. The silver halide crystals in the suspension are less than 3 μm in length, depending on the film type, and the emulsion layer is approximately 10 μm thick. Silver halide forms only about 20% of the volume of the emulsion layer. The size of the crystals contributes to the sensitivity and resolution of the film, as small crystals are less likely to be exposed, but also indicate more accurately the location of photon interaction. Furthermore, the number of emulsions influences the film sensitivity and resolution. If additional layers of emulsion are added, more crystals are present, thus

increasing the likelihood of a photon interacting within a crystal and later leading to a developed image. However, this also leads to a loss of resolution, as a single photon may be scattered within the first and second emulsions and produce two non-coincident development centers. [5]

A layer of hardened gelatin is placed over the emulsion layer to protect it from scratches while also providing a pathway for developing chemicals to reach the silver crystals. This layer is about 1 μm thick. In single emulsion films, the protective layer is only on one side, while the base forms the back side. In double emulsion films, the base is in the center of the film, and a protective layer is on both surfaces.

The gelatin used for the emulsion and protective layers is made largely of carbon, oxygen, nitrogen, and hydrogen. Importantly, these low-atomic number elements have small x-ray attenuation coefficients, and therefore have an inconsequential effect on the photon interactions in the silver halide crystals. Neutrons, however, can interact with nuclei of these elements and lead to reaction products (namely, protons from the $^{14}N(n,p)^{14}C$ reaction) which expose silver halide crystals. The silver in the film can also absorb incident thermal neutrons and decay via β- emission. Thus, the film is inherently sensitive to both types of radiation, although the exposure due to neutrons is only by an intermediary charged particle, and significantly lower than the sensitivity to photons. [4]

2.5.2 Theory of Latent Image Formation and Development

Although silver halide based photography was discovered in 1839, a comprehensive theory of the photochemical reaction occurring within the film was not constructed until 1938. Before this, scientists were aware that the primary component of

the developed image was metallic silver, and that an unknown process transformed the silver halide grains. The theory explains the formation of the pre-developed, or latent, image, and provided a framework to explain certain aspects of film performance to be discussed in Section 2.5.3. A second theory describes the development process, which transforms the hidden latent image into a visible one.

Silver bromide, the usual species of the silver halide crystals in film, exists in a face centered cubic crystal structure similar to common rock salt. The silver and bromine form an ionic bond, with the bromine becoming negatively and the silver positively charged. Impurities and interstitial silver cations are also present within the lattice structure. According to the theory, incoming photons liberate an electron from a bromine anion. If these primary electrons have sufficient energy, they can free additional electrons from other bromine atoms. Low energy electrons combine with interstitial silver cations to form metallic silver, while the uncharged bromine becomes gaseous and is absorbed by the gelatin of the emulsion. Collections of metallic silver atoms, known as sensitivity sites, are then used to catalyze a reaction which converts most of the silver within the crystal lattice to metallic silver, producing a developed image.

Early researchers realized by partially exposing and developing silver bromide crystals that deposits of metallic silver were found at discrete locations rather than dispersed evenly throughout the crystal. They also knew that impregnating the silver bromide grains with silver sulfide tended to increase the film sensitivity. It is believed that freed electrons traverse the lattice until they came to an electron trap, caused by either a dislocation in the lattice or a silver sulfide molecule. Once in the trap, the

immobile negative charge attracts free, interstitial silver cations. A silver cation then migrates to the trap, combines with the electron, and is reduced to metallic silver. [31]

According to [4], approximately 7 eV are required to remove an electron from bromine in the lattice structure. Visible light accomplishes this by the photoelectric effect, and therefore can produce a single electron (and therefore a single silver atom) per photon. Exposure by visible light requires many photons interacting within a relatively small area, as a single grain must contain at least five collocated silver atoms to form a sensitivity site capable of catalyzing grain development.

Higher energy photons, however, are more likely to Compton scatter and impart large amounts of energy to many electrons, and often in multiple grains. Consequently, it is not the direct action of the photon that exposes the grain; rather, the high energy Compton electrons passing through the lattice frees other electrons which travel to the electron traps and form metallic silver. A single Compton scattered electron within a grain can liberate enough secondary electrons via collisional interactions to make the grain developable. Importantly with regard to neutron radiography, high energy electrons generated outside the film and travelling into the emulsion layer can create a latent image by the same mechanism. Nominally, a single high energy (about 1 MeV) photon can lead to the creation of sensitivity sites in about ten grains. [31]

From this explanation, it may appear that the film is more sensitive to high energy photons than low energy photons, since many low energy photons are required to make enough metallic silver to catalyze development, but a single high energy photon can accomplish the same end. However, high energy photons also have a longer mean free path through the film, and the probability of interaction is much lower than for visible

photons. As a result, x-ray film is sensitive to visible light, and photographic film is sensitive to x-rays and gamma rays. The specific difference between the two types of film is proprietary. It is suspected that the crystals in x-ray film are larger and dispersed differently in the emulsion layer. Exact details, however, are unknown outside of the film manufacturers, and vary among film types and suppliers. [32]

Once the sensitivity sites are created on the surface of the grains, the film retains a permanent, though still sensitive and invisible, record of the photon interactions. Development transforms this into a stable, visible image. During the development process, developing chemicals are oxidized and transfer electrons to the silver cations still in the crystal lattice. However, this reaction cannot happen in the absence of the sensitivity sites. While the exact mechanism is still in doubt, it is hypothesized that the sensitivity sites on the surface of the grain act as conduction pathways for electrons to access and reduce silver cations in the lattice, thereby catalyzing the transformation from silver bromide to metallic silver. Filaments of black metallic silver form the visible and permanent image. After development, the bromine from the grains is carried away by the developing chemicals, and the remaining silver is retained in the emulsion gelatin. The film is no longer sensitive to radiation or light. Amazingly, the developer transforms a sensitivity speck of approximately ten silver atoms into the complex filament structure containing about 10^9 silver atoms.

After the developer creates the silver filaments, a chemical known as fixer is used to remove the remaining silver bromide grains which had no sensitivity sites, and therefore were not sufficiently, or at all, exposed. To do this, the fixer molecules combine with the silver cations to form soluble salts. Ideally, the fixer does not affect the

metallic silver filaments in the emulsion. A washing step in tap water removes the remaining silver salts, leaving a visible image. [31]

Because the development process is a chemical one, factors such as temperature, chemical concentration, time, and agitation can have enormous effects on the quality and level of development. High temperatures of the developer can cause the conversion of grains with no sensitivity sites, while high fixer temperatures may result in the loss of converted metallic silver. Automated processes are frequently used to standardize these parameters and prevent the loss of an image to improper development. [30]

2.5.3 Performance Characteristics

In a square centimeter of film, one could expect to find nearly two million silver bromide grains. Even though only a small fraction of these grains are exposed and developed, quantifying the exposure by the number of remaining grains is impossible. Therefore, in order to determine how much radiation exposed a film, the concept of film density was created. Film density is a measure of the ratio of incident versus transmitted visible light, as given by

$$D = \log\left(\frac{I_o}{I}\right) \tag{2.36}$$

where D is the film density, I_o is the intensity of the light incident on the film, and I is the intensity of the light transmitted through the film. [5] Obviously, density is a scalar quantity, and typically ranges between zero and five. Measurement of film density requires a transmission densitometer, which analyzes about 2 mm^2 of film per

measurement. [30] Densitometers can either be calibrated to the light from an x-ray film viewing box, or have an internal light source.

The relationship between film density and exposure is quantified in charts known as characteristic curves. [5] An example is shown in Figure 10. Importantly, the abscissa is logarithmic exposure, with exposure in units of quanta per unit area or time, if the exact flux is unknown. In neutron radiography, exposure is typically measured in neutrons/cm^2. These curves are generated by exposing a series of films to a known radiation fluence for increasing durations. The densities of the films are measured, and plotted versus the overall fluence (the product of the known flux and duration). [33]

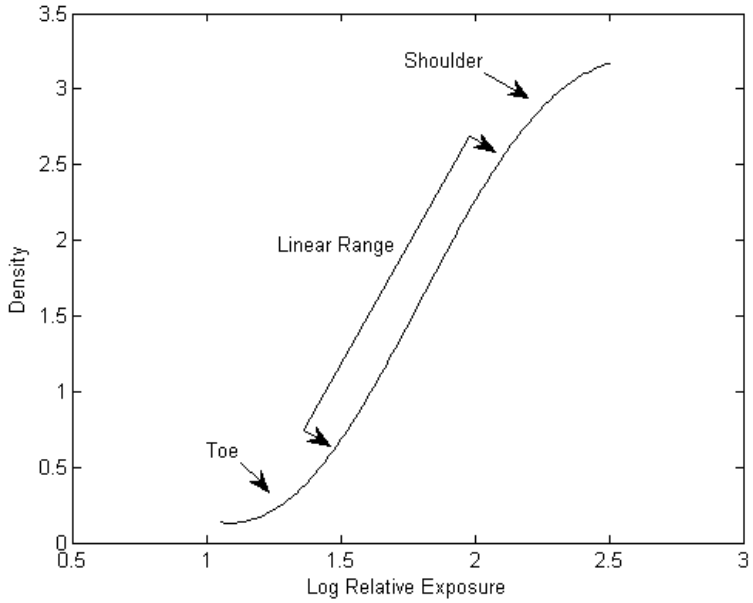

Figure 10 – Sample characteristic curve. [4]

Generally, the relationship between logarithmic density and logarithmic exposure (and, for that matter, the transmission ratio and ordinary exposure) is linear. At low and high exposures, this linearity fails. Through the linear range, incoming radiation of equal

energies will trigger the production of sensitivity sites in an equal number of grains. When a large portion of the grains have already been exposed, that is, when the exposure is high, the probability of incoming radiation interacting in unexposed grains becomes much smaller. Energy is then wasted on re-exposing previously exposed grains, explaining the formation of the "shoulder" in Figure 10. Film in this region is over-exposed. On the opposite end, partial development of unexposed silver bromide grains, film construction materials, and film handling and storage conditions contribute to a slight darkening of the film. This is referred to as background film fog, and indicates underexposure. [31]

Normally, the link between exposure and density is dependent on the total fluence, and independent of the magnitude of either the exposure duration or flux. This means that a film exposed to 10^9 photons/cm^2·s for 1 s will exhibit the same response as a film exposed to 10^8 photons/cm^2·s for 10 s. This behavior is known as the Bunsen-Roscoe reciprocity law. [31] However, during photography of extremely low-intensity astronomical objects, it was observed that the law of reciprocity failed when the flux was abnormally low or high. [34] This deviation is known as the Schwarzschild law. In the case of low intensity exposure, the likelihood of rapid photon interaction within a single grain was relatively low. Thus, the first atoms of metallic silver were likely to lose electrons and revert to silver cations before more atoms could join and create a sensitivity site. For high intensity exposure, electrons flood the electron traps, producing a repulsive force that disperses the electrons before silver can migrate and neutralize the charge. This also prevents the creation of sensitivity sites. [31] This phenomenon is only observed when the electrons combining with silver cations are formed directly by

individual photons. When charged particles trigger this reaction, many electrons are produced over large area and are therefore capable of preventing both effects. Charged particles registering in the film are assumed to obey the reciprocity law. [8]

One advantage of plotting the characteristic curves on a logarithmic scale is that ratios of film exposures are reflected by a constant distance between curves. That is, a film twice as sensitive as a baseline will appear two logarithmic units of exposure to the left, and a film half a sensitive as the baseline curve will appear two units to the right. The location along the abscissa is known as the film speed, and is given relative to some arbitrary baseline. If the characteristic curves of a variety of films are plotted on the same axes, films with curves farther to the left are faster than films to the right, indicating that a lower exposure is required to achieve the same film density. Another film characteristic that can be interpreted from the characteristic curve is the inherent film contrast, based on the curve slope. A steep curve indicates that a small change in exposure will result in a drastic change in film density, while a shallow curve requires a large change in exposure for a small change in density. [4]

It should be noted that when a specific film is tied to a specific neutron conversion screen for use in neutron radiography, the combination of the two produces a unique characteristic curve that reflects all of the processes involved. This includes the neutron absorption efficiency in the converter material, the secondary radiation production rate, the transfer of reaction products into the emulsion, and the efficiency of the reaction products registering within the emulsion.

III. Experimental Approach

3.1 Detector Construction

The detector is an assembly of an aluminum frame, gadolinium oxide, Mylar, and film. The assembly is wrapped in aluminum foil to seal out ambient light which could expose the film. A Beam Purity Indicator (BPI) is secured to the foil directly over the film using thin tape, and the entire assembly is vacuum sealed in a polyethylene and nylon package. A schematic with dimensions is shown below in Figure 11, and an exploded view is in Figure 12.

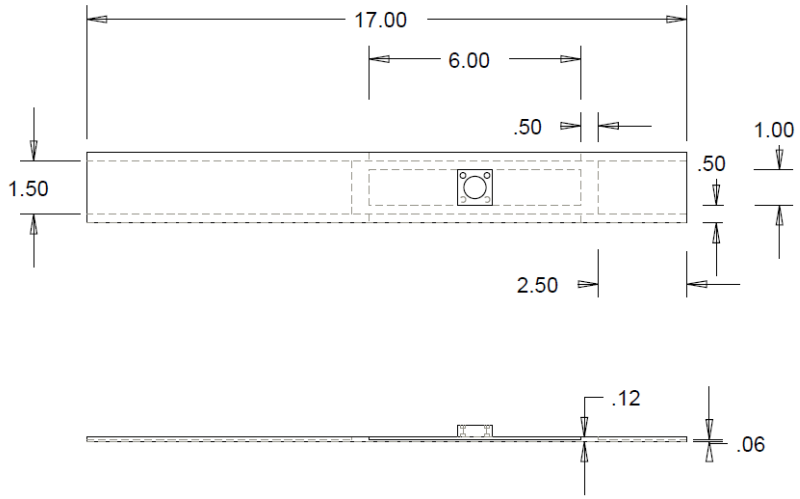

Figure 11 – Schematic of detector design. All units are in inches. The materials used were produced in standard measurements; these have been retained for consistency.

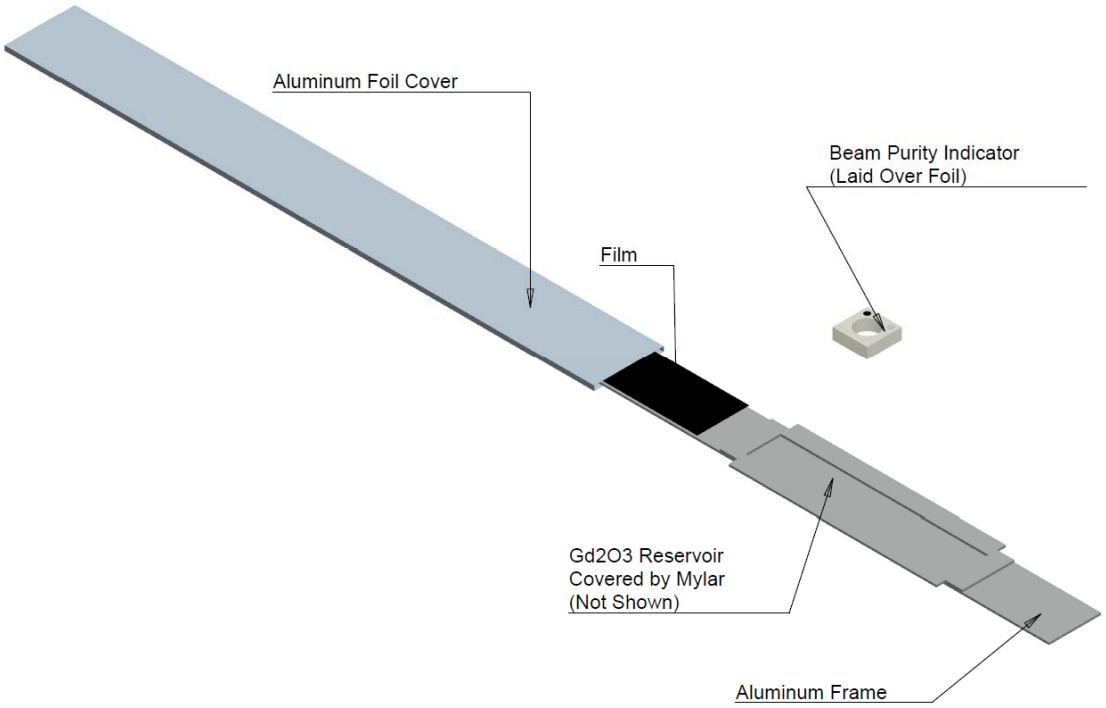

Figure 12 – Exploded view of an assembled detector.

Aluminum was chosen as a suitable base and ambient light sealant due to its low thermal neutron absorption cross section of 0.231 b. [35] It is anticipated that, because of this low cross section, the aluminum will not have a significant effect on neutron flux. Furthermore, because aluminum is a low-Z element, it should have little impact on any gamma radiation. The frame width was chosen to fit within a 2 3/8 in deep well running along a stringer in the AFIT thermal neutron source (see Figure 14 below), and the length matches the length of the supplied x-ray films. The frame was constructed of an aluminum bar 1/16 in thick and 1 1/2 in wide, as commercially available. The reservoir is framed by narrower pieces, 1/2 in wide, adhered to the base with cyanoacrylate glue. It was designed to be wide enough to accommodate a BPI. After filling the reservoir, the

edges were sealed with electrical tape. This tape and the vacuum sealed envelope are not shown in Figure 12.

Two detector frames were constructed. A small piece of spare aluminum was placed in the corner of one reservoir to differentiate the detectors.

Agfa Structurix D7 x-ray films were trimmed to fit onto the base. It is one of the most sensitive films made by Agfa. It is commonly used for neutron radiography, and is of similar performance characteristics to other film types used in the field. The manufactured films were 7 in by 17 in. Each production film was trimmed to produce four 1 1/2 in by 17 in strips for irradiation.

A single layer of consumer grade aluminum foil is wrapped around the assembly after the film is added, and the BPI is secured to the aluminum surface directly over the gadolinium oxide powder reservoir. The package is fitted into a FoodSaver vacuum sealing bag, approximately 2 1/2 in wide and greater than 20 in long. The vacuum ensures intimate contact of the film, converter, and BPI during irradiation.

It must be noted that the construction of the detector must be performed in complete darkness to avoid exposing the film. An advantage of the aluminum foil wrapping is that it allows the film to be placed and quickly insulated against light. The package can be taken into a lit room, where the BPI is secured and the assembly vacuum sealed.

The PTFE blocks for the BPIs were obtained from Industrial Plastic Supply, Inc. The lead and boron nitride disks were provided free of charge by the Victory White Metal Company and St. Gobain Ceramic Products, respectively.

3.1.1 Converter Design

The design of the converter was particularly important, and one of the essential points of this research. While gadolinium is a highly efficient material for conversion construction, it has a few disadvantages. First, the material is relatively expensive. Second, and more importantly, gadolinium spontaneously oxidizes in air, and forms flammable hydrogen gas when exposed to water. Shipping gadolinium is difficult. [36] It is therefore desirable to use gadolinium in compound form for chemical stability.

The methods used in this research were motivated by the successes reported in [10]. Lima found that gadolinium in compound performed nearly as efficiently as pure gadolinium. Specifically, she converted gadolinium oxide powder to gadolinium chloride by reaction with hydrochloric acid. This was then dissolved in a fingernail polish and acetone mixture. The solution was sprayed over an aluminum foil base and allowed to dry. The constructed converter was employed as any other metallic converter, and produced comparable neutron radiographs.

The materials were carefully chosen in that research, but the rationale for some of the choices was questionable. Gadolinium chloride was used because the researchers were afraid the high scattering cross section of the oxygen in gadolinium oxide would decrease converter efficiency. [10] However, this is incorrect. The scattering cross section of oxygen over all isotopes is 4.232 b; for chlorine, it is 16.8 b. [35] Therefore, to minimize the interference of chlorine atoms, and to eliminate the difficulty of working with hydrochloric acid, it was decided to use pure gadolinium oxide.

Lima's choice to use fingernail polish to seal the gadolinium chloride was also questioned. While it allowed for a solid and stable conversion layer, it is impossible to

know if the gadolinium chloride (or, here, gadolinium oxide) grains were homogenously mixed within the substrate. The grains of the oxide could have a higher density than the nail polish, and descend to the bottom of the layer. Furthermore, it would be difficult to ensure that subsequent layers sprayed over previous ones would be of the same thickness. Finally, the exact composition of the fingernail polish would be difficult, if not impossible, to ascertain, and therefore its effect on neutron and electron flux was determined to be unpredictable.

A mechanism was still needed, however, to ensure that the gadolinium oxide would be physically stable and prevented from sticking to the film surface. The separation layer would have to hold in gadolinium oxide powder, be resistant to small abrasions, and permeable by electrons. Non-aluminized Mylar was chosen to suit these needs. The Mylar used in this research is 23.4 μm thick. Free samples of this material were provided by Piedmont Plastics. As noted in Section 2.4, the range of electrons through this material is between 26 and 82 μm, depending on the estimation method used. Using the exponential attenuation approximation for the range of electrons in Mylar, and taking the mean free path to be the expected ranges provided in Section 2.4, between 25% (for an expected range of 82 μm) and 60% (for an expected range of 26 μm) of the 71 keV electrons will be attenuated. Thus, while a large fraction of the electrons will be attenuated in the Mylar, a significant portion will remain to expose the film.

The gadolinium oxide powder thickness was chosen to be approximately 1600 μm. This corresponds to the 1/16 inch thickness of available aluminum pieces forming the frame. The thickness proved to be fortuitous. Based on the analysis outlined in Section 2.1.2 and illustrated in Figure 13, it was determined that this thickness would

provide near-maximum converter efficiency. To determine the amount of gadolinium oxide used, the frame mass was measured before and after filling the reservoir. For both frames, the beginning mass was 95.0 ± 1 g, and the end mass was 105 ± 1 g. The total mass in the reservoirs is then 10.0 ± 1.44 g. The density can be ascertained as well using the reservoir dimensions and uncertainties. The uncertainties in length and width are taken as 1/32 in, or 0.08 cm, from the measurement resolution. The uncertainty in thickness is estimated as 25% of the total thickness, or 0.04 cm. The volume is then 6.15 ± 1.6 cm^3, and the density is 1.63 ± 0.47 g/cm^3. While this is a large uncertainty, the converter efficiency is relatively insensitive to this quantity, as shown in Figure 13. As a side note, the reservoir was repeatedly filled and sealed under vacuum to increase the quantity and density of gadolinium oxide. This also created a stable and solid layer, as opposed to loose powder. The seal was released, and more gadolinium oxide added to compensate for the void created by the compacted powder. This process was repeated three times, until no more compaction was observed with subsequent vacuum sealing.

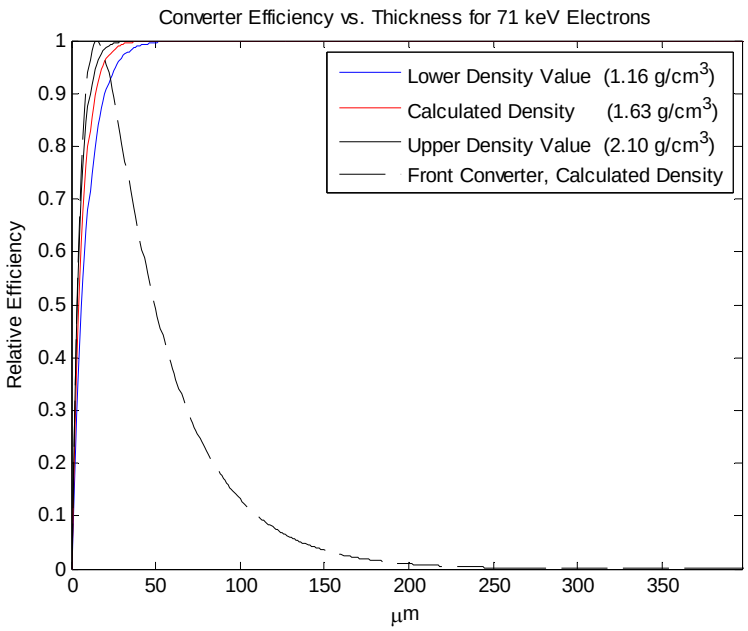

Figure 13 – Front and rear converter efficiencies as a function of converter thickness. The macroscopic neutron absorption cross section is centered on 0.0264 μm^{-1} [37], based on a density of 1.63 g/cm^3, and then recalculated for the bounding uncertainties. The electron attenuation parameter is 0.1344 μm^{-1} as calculated by the inverse of the mean range equation (2.35) with K = 11.5 and n = 1.35, and scaled similarly.

Figure 13 shows the effect of thickness up to a quarter of the true thickness (397 μm). Thus even if the layer were 25% as thick as expected, it would still provide effectively the same efficiency of electron production and transport. Making the layer very thick, and using it as a rear converter rather than front, renders the converter efficiency insensitive to small variations which would be very difficult to measure. Furthermore any thickness deficiency which would result in appreciable efficiency losses would be very obvious to the naked eye. The uncertainties in density have little effect on the overall efficiency, especially at higher thickness values, and uncertainties in thickness have little effect when the rear arrangement is used.

3.2 Film Response Characterization

Every characteristic curve presented in the cited works shows a film density linearly related to neutron fluence over several orders of magnitude. Although these sources used pure metallic foils rather than compounds, the x-ray film here was expected to respond similarly. As in Figure 10, a base film density was expected due to film construction materials and background exposure. Above a fluence of approximately 10^8 neutrons/cm^2, the film was expected to begin to saturate.

Irradiation was performed using drawer three of the AFIT graphite pile. According to calibrations [17], thermal neutron flux is highest in this location. However, a key disadvantage of using the graphite pile was the nondirectionality of the thermal neutrons. Thermal neutrons in the pile are diffuse and behave like a gas, making the flux direction random. Figure 14 illustrates the arrangement of the detectors in the milled graphite stringer, and Figure 15 shows the relative locations of the source and detectors. Figure 14 demonstrates that the sensitive regions of the detectors were placed facing outwards. This was to prevent one detector from shielding the other.

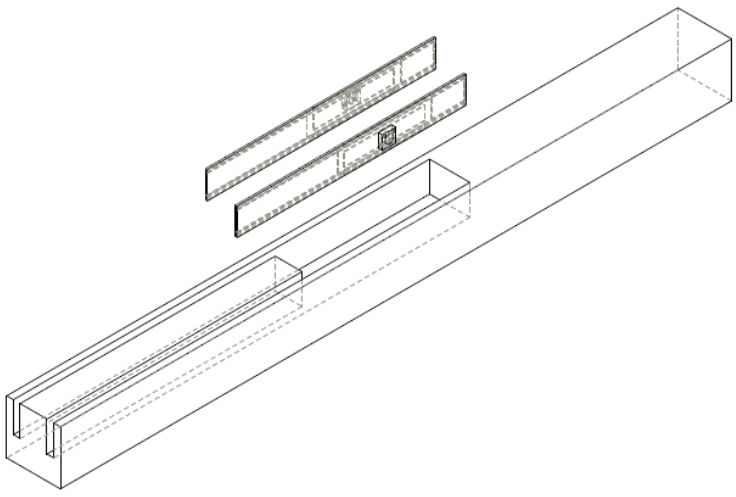

Figure 14 – Arrangement of detectors in milled stringer.

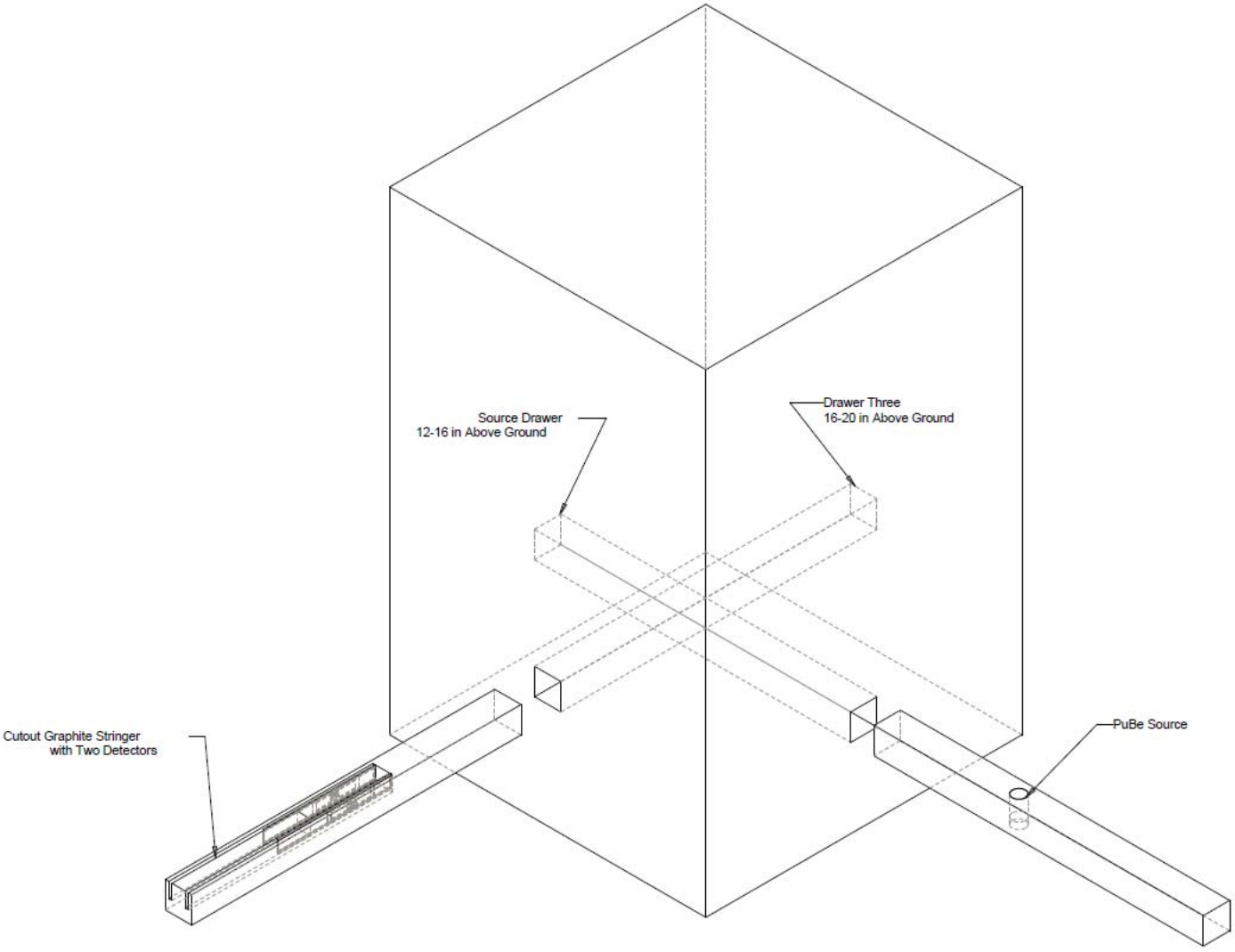

Figure 15 – Relative positions of the source and detectors in the pile. When the stringer is fully inserted, the detectors are directly over the source.

Flux was considered constant for all test points. Therefore, irradiation time was varied to obtain the desired fluence. Flux measurements reported in [19] were used to calculate the total fluence for the pile configuration. Furthermore, the source strength calculated in [19] of 1.01×10^{7} n/s was assumed.

The referenced calibrations of the pile, however, were performed using activation foils. Activation foils can capture neutrons incident from any direction. The detectors used here are monodirectional; that is, neutrons entering from the rear cannot contribute to film exposure. Additionally, since the thermal neutrons are diffuse and behave similarly to a gas, no large element of directionality would be retained. Therefore the value of 9028 $n/cm^2 \cdot s$ for the thermal neutron flux in drawer three was halved, and this value (4514 $n/cm^2 \cdot s$) was multiplied by the total irradiation time to obtain the fluence. Uncertainty was treated similarly.

Films were developed using a developing machine to standardize chemical temperatures and times. The developing machine, an Agfa Gevaert NV model 9462/846 was provided courtesy of the Enon Veterinary Hospital. Chemical temperatures were automatically controlled by the machine. Dryer temperature was the only available setting, and was set to five for the all development. (Dryer temperature can be adjusted for local humidity and temperature; while the exact relation between setting and temperature is unknown, the machine had been optimized by the veterinary assistants for use in the practice.)

Film density measurements were performed in the BPI regions specified by Table 2, five locations equally spaced along the center of the reservoir length, and locations at the same longitudinal location, but outside of the reservoir area. Interior locations were measured five times in an attempt to negate the effect of developing marks observed during preliminary trials and shown later in Section 4.3. A similar approach was impossible for the areas outside of the reservoir because the margins outside the reservoir were not large enough. Locations were indexed from left to right. Point 1 was furthest

from the source, and point 5 was closest. An illustration of the measurement locations is shown in Figure 16. Data points were not averaged; rather, each film yielded a total of 25 measurements, all of which were retained for data analysis.

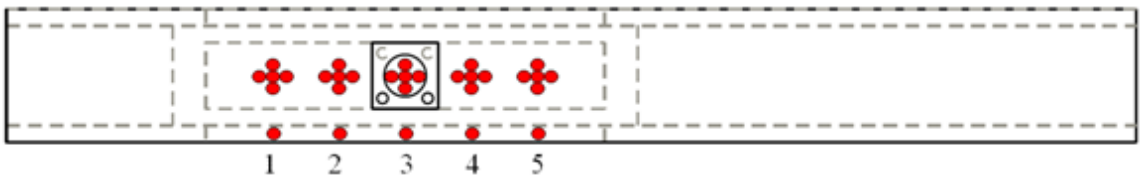

Figure 16 – Locations of measurements along film length made in addition to those required for the BPI.

Performing measurements in this manner gave paired gamma and neutron readings. Any axial variation in gamma or neutron contribution could therefore be identified with this data. In practice, the margins outside of the reservoir were sometimes too thin on one side to take a measurement. In these cases, measurements were taken on the opposite side.

Values of film density were recorded using a bright light source and an Eseco Speedmaster SM-14 film densitometer. The densitometer is a small hand held device with a 3 mm diameter measuring area protruding from one side. The device is accurate to ± 0.02 density units. Before taking measurements, the densitometer was zeroed to the light source baseline and calibrated using the manufacturer's supplied calibration strip. This ensured accurate and proportional readings between 0.00 and 3.29 density units. To take the BPI measurements, the film was secured to the light source using tape outside of the measurement area, and necessary BPI regions visually identified. The densitometer was placed over these regions, and the measurement taken. A guide was created to

quickly make the other measurements by punching holes in a discarded film envelope in the appropriate locations. This guide was secured to the light source, and films aligned individually inside. The densitometer was slid between each of the points, and readings were recorded. The device calibration was confirmed after twenty measurement intervals.

Films were irradiated in approximately half decade time increments, from 10^2 to $10^{5.5}$ s. (The next step, 10^6 s, would have required 11.5 days of irradiation time.) The order of irradiations was pseudo-randomized to reduce the possibility of a systematic unknown contribution such as processing, handling, or exposure by ambient light and radiation. True randomization was sacrificed for safety when necessary – that is, detector retrieval at unusually late or early hours was avoided. Films were irradiated in pairs, and two replicates of each data point were performed, for a total of four films per irradiation duration. This was not performed for the very low irradiation points which, after one replicate, showed no film density above background.

Control films were also exposed. These films were handled and processed nearly identically to the test films, but were not irradiated. Because they came from the same stock of films, they were expected to behave identically to the other films in the batch, and therefore provided a representative baseline. The average film density of these films, recorded in a similar pattern to Figure 16, was considered a measure of both the ambient light in the dark room during assembly and development and film construction density. Four film strips were developed, and the average density was subtracted from the measured densities of the irradiated films.

A linear relationship between density and irradiation time for a constant flux was expected, as reported in Section 2.5.3. Unfortunately, performing a simple linear regression on the data was not appropriate, as the independent variable sometimes had significant uncertainties. There were two sources of this uncertainty. First, the time required to put the detectors in place was not included in the target irradiation time, but the detectors could conceivably register radiation arriving during this time. For all data points, the time to put in place and remove was taken as 40 s. The second source of was due to the uncertainties intrinsic to the calibration, such as counting statistics and detector efficiencies, which was coupled with the uncertainty in irradiation time to obtain an uncertainty in neutron fluence.

A strategy of weighting data points by the inverse of their respective uncertainties was devised. Since there were errors in both the independent and dependent variables, both needed to be taken into consideration when weighting. However, the error in density measurements was constant for each point, and would not give any indication of more or less accurate data points. Uncertainty in time and flux, coupled as the uncertainty in fluence, was used to weight. Another complication was encountered, though, in that the errors were linear, but the independent variable was logarithmic. That is, an irradiation of $10^{5.5} \pm 40$ s is a much more accurate data point than $10^{2} \pm 40$ s. Since $\log(x+y) \neq \log(x) + \log(y)$, the error was treated as the difference between the logarithm of the data point and the logarithm of the data point with error, as below:

$$\begin{aligned} \text{Error} &= \log\left(x+\sigma_x\right) - \log\left(x\right) \\ &= \log\left(\frac{x+\sigma_x}{x}\right) \end{aligned} \tag{3.1}$$

After simplifying the logarithms, the defined error became the logarithm of the relative error. The inverse of this value, normalized over all of the weights, was considered to be the weight of each data point, so that the data point with the lowest error was given a weight of one, and data points with high errors were given lower weights.

The toe region of the characteristic curve was identified as beginning when the film density increased above the background, as determined by the control films. The shoulder region was planned to be considered as 90% of the asymptotic density; however, film saturation was not conclusively reached with the irradiation times used. Therefore, all data points above the film background density were used for linear regression.

3.3 Assumptions

Some of the necessary assumptions have been outlined previously in this document; however, a concise presentation with justifications is prudent.

It was assumed that the flux and uncertainties measured in [19] are still accurate, despite being approximately 2 years old. While fluxes increased by approximately 30%, this increase was over 50 years. Approximating this by a linear growth, the reported values from 2010 are only off by about 1%, which is significantly lower than the uncertainties reported with the original numbers.

The chemical bond between gadolinium and oxide was considered to have no effect on the emission of conversion electrons. This was because conversion electrons come from the K, L, and M shells. The most common, the 71 keV electron from Gd-158, is an L shell electron. However, these interior shells do not participate in chemical

bonding. While these electron clouds may be distorted, it was assumed that these interior shells are unaffected by the chemical bond.

Because the films are being developed automatically, sensitive development parameters, such as temperature, time, and agitation, were considered constant. Environmental factors before development such as temperature, humidity, and duration were considered as part of the constant film background.

The layers of vacuum sealing material and aluminum foil were assumed thin enough to not significantly affect the neutron flux. This is because the macroscopic cross section for absorption in aluminum is 0.0138 cm^{-1}, and polyethylene (the main component of the vacuum material) is 0.010 cm^{-1}. [37],[5] Over the thickness of the aluminum foil, 0.016 mm [38], and the vacuum bag, 0.1 mm [39], this corresponds to an attenuation of less than 1%.

A certain but significant number of fast neutrons entered the detector without being fully thermalized. This is based on the large cadmium ratio recorded in [17] for drawer three. It is assumed in this research that these fast neutrons had little effect. The absorption cross section of epithermal neutrons (~ 1 keV) is approximately 100 b in Gd-157, and 10 b for fast neutrons (100 keV). Resonances in the important isotopes (Gd-155 and Gd-157) are all below approximately 300 eV. These cross sections are compared to the 255,000 b cross section for thermal neutrons. [21] While some higher energy neutrons may be absorbed, the fraction of total absorptions by higher energy neutrons should be small. Furthermore, the x-rays that accompany the release of a conversion electron (and which could expose the x-ray film) will be taken as part of the fundamental

neutron conversion process. Any additional exposure by these x-rays will be directly tied and proportional to the exposure by conversion electrons.

Any activation of silver atoms in the film and their subsequent decay will be assumed to not contribute to film density. This is based on the low cross section of silver compared to the gadolinium, and corroborated by experimental evidence that the film exposed while over the gadolinium reservoir had higher densities than the adjacent areas. Additionally, the probability of an electron emitted isotropically within a thin layer and then interacting in the same thin layer is low, as the electron has a high probability of escape.

Finally, it was assumed, as with [8], that film exposure by electrons is independent of the rate of exposure; that is, the Schwarzschild effect was not present.

IV. Results

A clear pattern of increased film density with increased irradiation time was observed. Unfortunately, the thermal neutron source employed during testing was not optimal and rendered the BPI useless. Other problems with film stability and consistency were noted. Nonetheless, film contributions were separable, and a linear regression was performed which characterized the film response to neutron fluence.

4.1 Source Characteristics and Effects on Results

It was determined that the flux in the graphite pile was not directional enough to use the BPI. This was concluded from the relative densities of the pertinent areas of the BPI image. The density of the film behind the boron closest to the film was lower than the surrounding region, indicating that neutrons were blocked by the boron, and that neutrons were indeed responsible for some fraction of the film exposure. (See images of developed films in Appendix A) However, the density of the film behind the boron farthest from the film was equal to the surrounding region. This indicated that this boron disk did not significantly block neutrons exposing the film. This exposure pattern (low exposure behind nearest boron disk, no exposure change behind farthest boron disk) leads to the conclusion that the vast majority of the exposure was due to scattered neutrons. The equations in Table 2, specifically the calculation of direct thermal neutron content, yield negative contributions. If the fluence had retained some element of directionality (for instance, if it had been well collimated), then the images behind both boron disks

would have had nearly equal densities. It was impossible to create a directional thermal neutron beam in the graphite pile with a high flux using an isotopic source. Therefore, a reactor is necessary to produce a thermal neutron flux high enough to provide short irradiation times even after losses from collimation. This, in turn, is necessary for the BPI to be useful.

Additionally, precisely positioning the densitometer over the necessary points on the BPI proved extremely difficult, as the points were so faint. Therefore, the BPI method of separating exposure contributions was abandoned. Useable data was taken from the points as illustrated in Figure 16. Gamma contributions were determined from measurements made off from the reservoir, and neutron contribution was taken as the difference between measurements in the reservoir and the associated gamma measurement.

4.2 Characteristic Curves

Before characterizing the irradiation contributions to the films, background film density was determined. Figure 17 shows the recorded densities from four films exposed to the same darkroom, handling, and development conditions as the irradiated films. The four films were measured at five points centered axially along the film length and separated by 1 in.

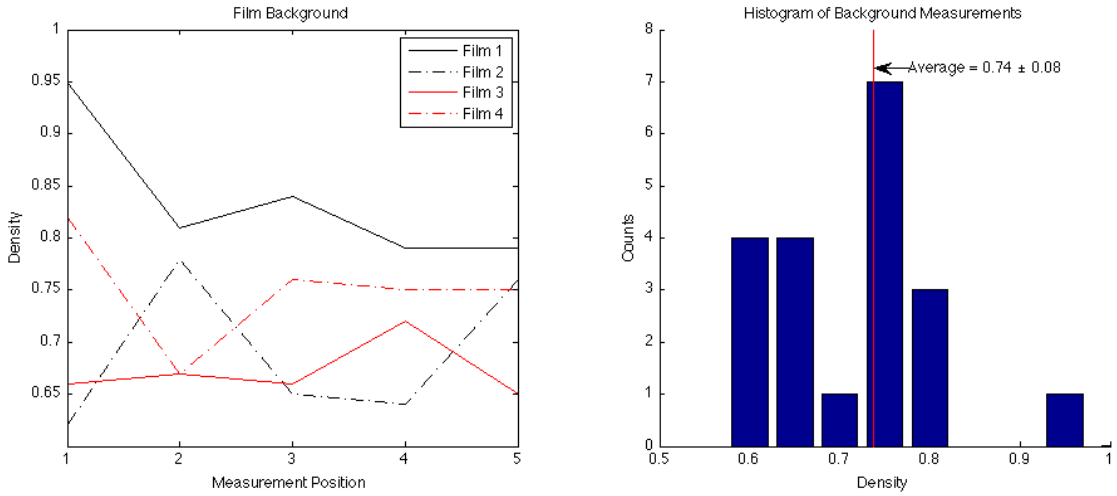

Figure 17 – Film background measurements.

The average background density was determined to be 0.74 density units, with a standard deviation of 0.08. This included any exposure due to ambient light during detector assembly, increased density caused by environmental conditions during storage (such as humidity and temperature), and the density of the film construction materials. No pattern was identified, and the distribution of the twenty data points did not appear to follow any trend. Because all of the films came from the same batch, the average of the measurements was taken as being representative of the background for every film.

Figure 18 shows the raw density measurements before removing background for each of the 21 films used. Note that many films were discarded due to development issues, to be discussed in Section 4.3.

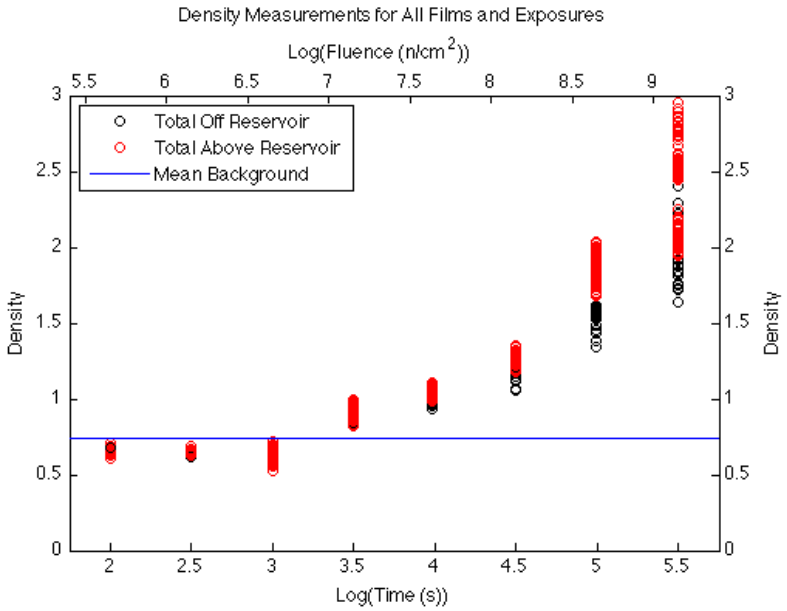

Figure 18 – Recorded measurements for all films. Densities off reservoir were due to gamma contribution; densities in reservoir were due to neutron fluence and gamma contributions. Two x axes are used to emphasize that gamma contribution was not due to the neutron fluence. Since log(fluence) = log(flux) + log(time), the two axes are offset by log(flux) = log(4514 n/cm^2·s) = 3.65.

A few remarks can be made about the data presented in Figure 18. First, low time/low fluence points showed densities below the mean background. This is because the films used for background measurements were deliberately left unsealed in the darkroom for a longer time than irradiated films to ensure a conservative estimate of background. Films used for data were exposed to ambient light for approximately a minute; films used for background were exposed for approximately two minutes. However, while density is linear with the logarithm of exposure time, the difference cannot simply be scaled. This is because the measurements contain a constant, but not directly measured, density due to film construction materials that is independent of exposure time. Furthermore, most of the low irradiation points fell nearly within one standard deviation of the background.

Also, Figure 18 shows that the increase in film density occurred due to increases in gamma and neutron interactions. Off reservoir measurements, representative of gamma content, were principally responsible for the increased densities. On reservoir measurements, indicative of neutron contribution, were higher, but did not increase as rapidly as gamma contribution.

Finally with regard to Figure 18, a wide spread of data points is obvious for each exposure point, varying by nearly one entire density unit. It was hypothesized that a pattern was hidden within the wide spread. Specifically, the fluence, both gamma and neutron, may have varied along the length of the film. Net gamma content (off reservoir measurement minus mean background) and net neutron content (on reservoir measurement minus its correlated off reservoir measurement) were plotted versus time and fluence, respectively. The measurement location information was retained, as shown in Figure 19.

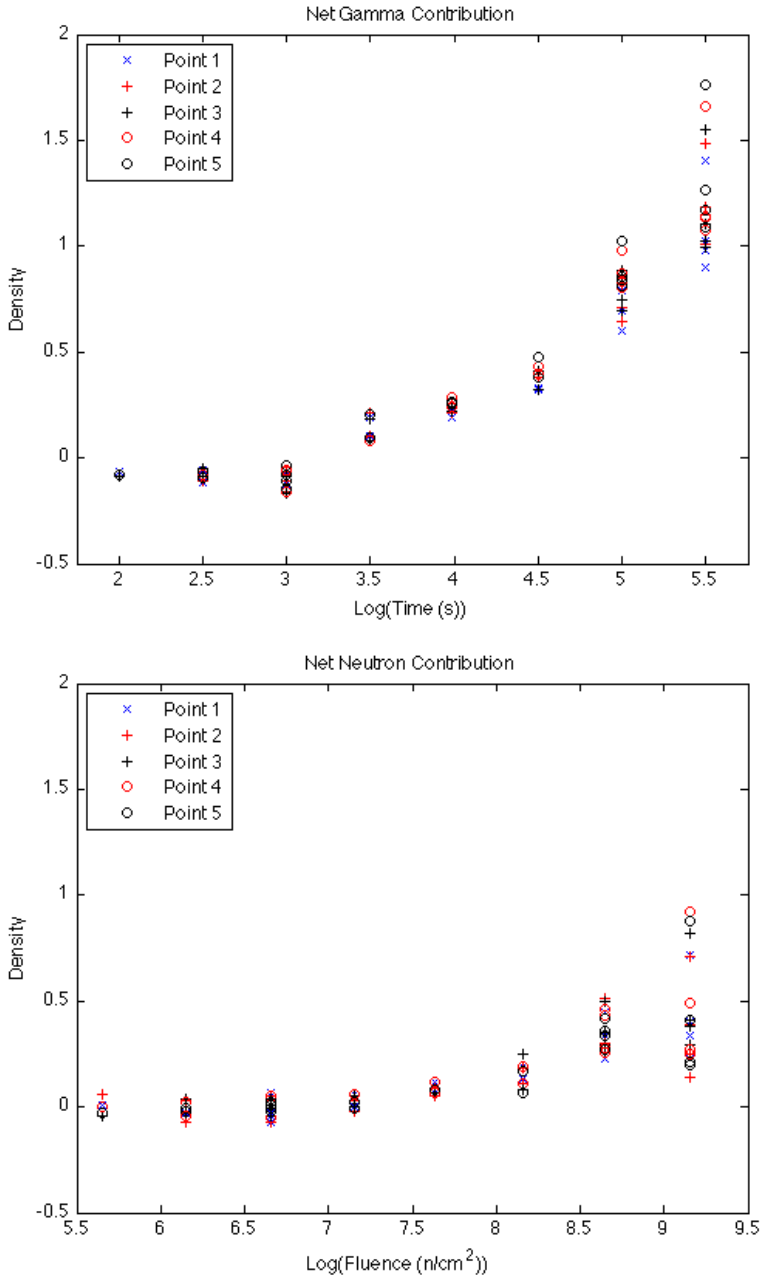

Figure 19 – Net neutron and gamma contributions, ordered by measurement point. Point 1 was farthest from the source axis; point 5 was closest to the source axis.

A pattern was observed for net gamma contribution that the observed densities for points closest to the source were consistently higher than points farther from the source. No similar pattern was observed for neutron contribution. Gamma rays from the source

are only slightly attenuated by the graphite in the pile, as carbon is a low-Z material. The gamma rays are therefore subject mostly to $1/r^2$ reductions. Since point 1 is approximately 9 cm farther from the source than point 5, it received a lower gamma dose, explaining the fairly consistent ordering of densities. The same pattern, however, was not observed for neutron induced densities. This is because neutrons in the graphite diffuse similar to a gas, and do not obey a $1/r^2$ reduction. Therefore, it was concluded that the gamma ray flux was not constant along the film, but neutron flux was nearly constant, allowing further examination of the dependence of neutron induced density on neutron fluence using all data points.

Similar to results published in [4] and illustrated in Figure 10, a toe and a shoulder region were expected in the characteristic curve derived from these results. In the toe region, the largest portion of film density would be due to background radiation and film construction materials. Here, photon and electron interactions would be so infrequent that sensitivity sites capable of catalyzing development would rarely form. In the shoulder region, the film would be saturated, indicating that individual grains were being re-irradiated and subsequent quanta would be wasted.

A clear toe and shoulder region were not observed in the neutron induced characteristic curve. Weighted linear regression was therefore performed on the data points which, from Figure 18, showed observable density above background. A total of 14 films with irradiations greater than 10^7 n/cm^2 were used in the regression. The results are shown in Figure 20.

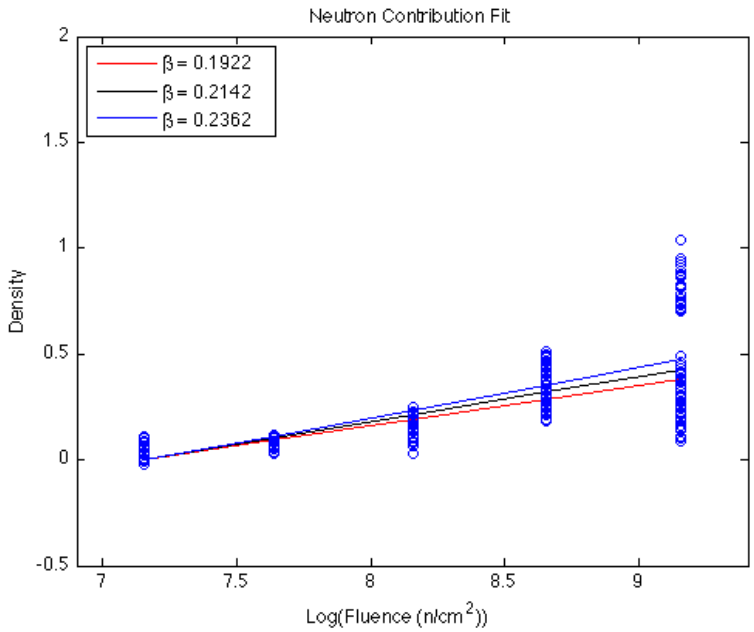

Figure 20 – Linear regression on neutron induced density.

A linear regression was performed on the data because density is assumed to behave linearly for a certain range of logarithmic exposure, namely, above the toe and below the shoulder. [4] Determination of these bounds is admittedly arbitrary. It may be that the poor linearity observed is due to inclusion of points which are better suited to the toe region. This cannot be stated with certainty, however, unless a finer resolution of data points is obtained. This was not performed here. Instead, extra data points were taken for similar exposures to examine measurement repeatability.

Figure 20 includes the 95% confidence limits on the slope of the curve. A similar examination of the gamma characteristic curve cannot be performed, as the gamma flux was unknown and not constant along the length of the film. The regression provided a coefficient of multiple determination (R^2) value of 0.51; however, because the data were weighted, the R^2 is not a reliable metric of goodness of fit. Regardless, from visual inspection of the data, the regression does not predict densities with great reliability.

Finally, the statistical behavior of the measured data points was examined for each irradiation setting. Histograms of the data, made with a bin size of 0.05 density units, are shown in Figure 21, and an overall trend of mean and standard deviation illustrated in Figure 22.

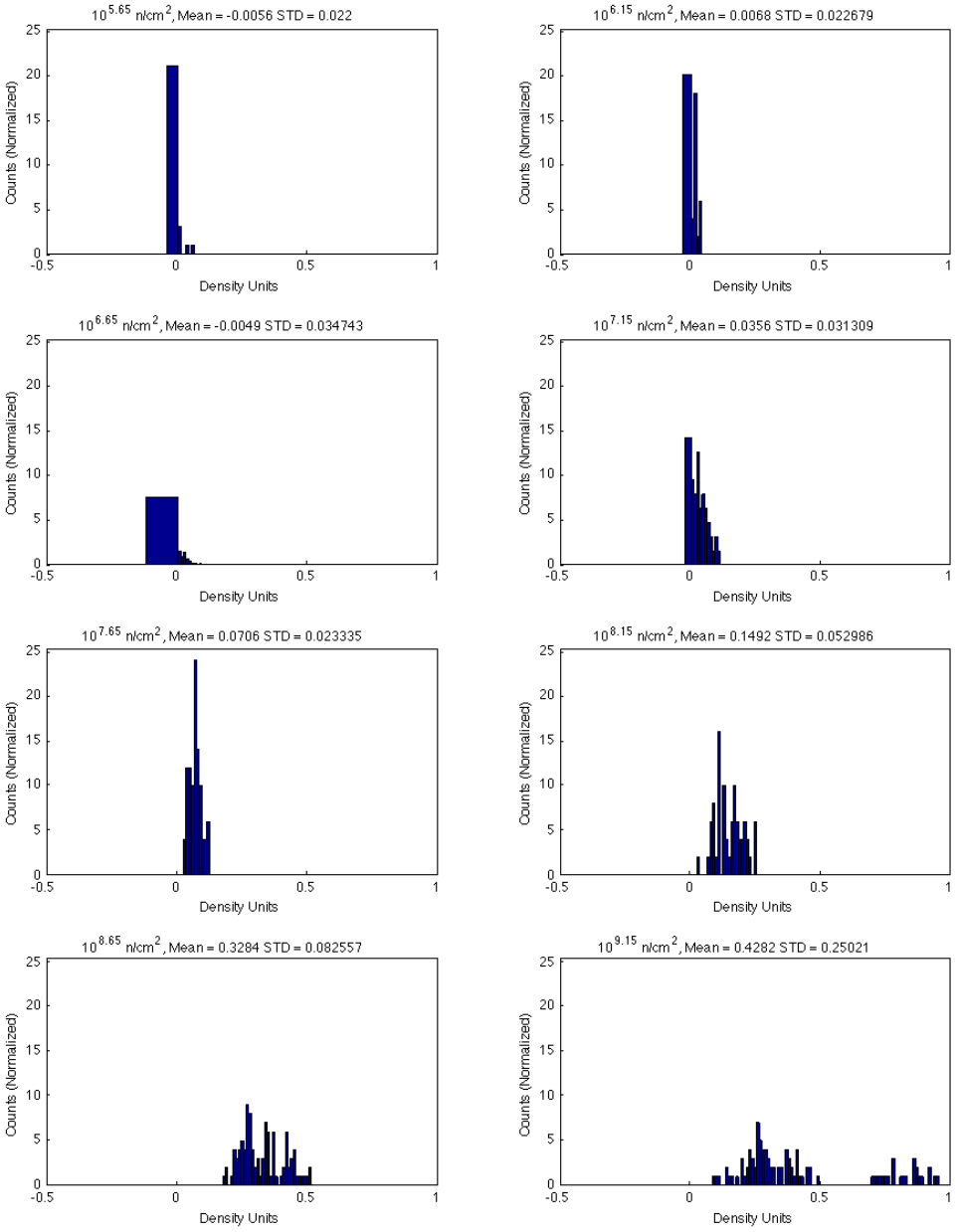

Figure 21 – Histograms of net neutron measurements of each tested fluence.

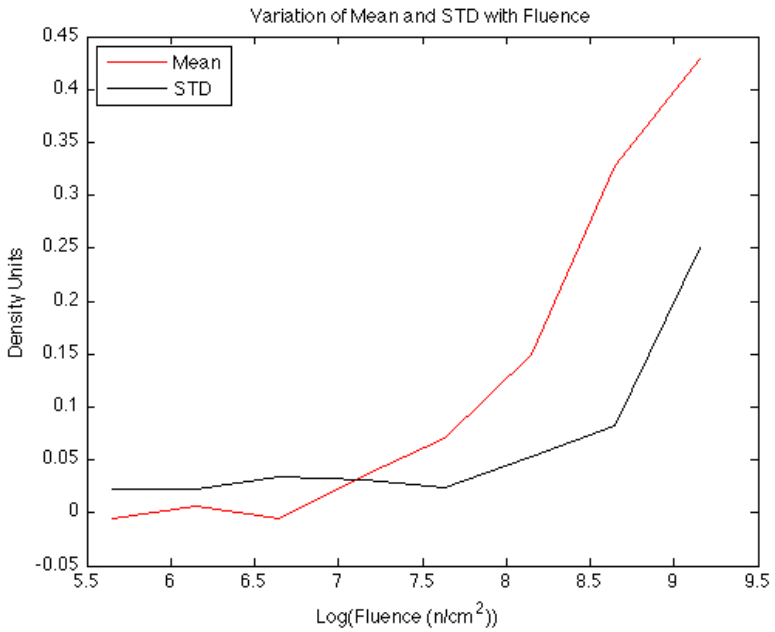

Figure 22 – Summarized data from the histograms presented in Figure 21. Both the mean density measurement and standard deviation rise monotonically after reaching the threshold fluence of 10^7 n/cm^2.

Low fluence test points exhibited a nearly flat distribution of densities, similar to the pattern observed in Figure 17. Variance in these low fluence data points was nearly constant up to approximately $10^{7.5}$ n/cm^2. However, above this fluence, the measurements began to display what appears to be a Poisson distribution, indicating that the probability of an interaction in the film is small and independent of time [14], and thus validating the assumption that the Schwarszchild effect is negligible. As expected from a Poisson process, the variance increases with the mean. This leads to the conclusion that measurements of higher fluences would be more inaccurate. Finally, the data for $10^{9.15}$ n/cm^2 shown in Figure 21, indicates that, aside from Poisson statistics, the film responds very differently to similar fluences. In this histogram, there appear to be two separate distributions. This could have been caused by slight differences in handling,

processing, and storage, but intimates that the film is unpredictably sensitive to many factors aside from the fluence.

4.3 Notes on Detector Performance

In one detector, the gadolinium oxide base separated despite repeated compacting during construction. The exact cause of this is unknown because it was not observed in both detectors, but the separation is suspected to be the result of further compaction during testing. Some of the powder then migrated to the areas under the electrical tape, resulting in less powder being present in the reservoir. This was only observed in one half of the reservoir, and so the detector was considered functional as long as the BPI was placed over the solid powder base. The half that had lost powder was obviously thinner when vacuum sealed than the unaffected portion of the detector. Only a qualitative comparison of thickness was noted, because measurement would require destruction of the detector. Nonetheless, these regions showed similar film densities to intact regions, as reflected by the random distribution of neutron densities with respect to measurement location in Figure 19, validating the derivation from Section 2.1.2.

A calculation of detector efficiency in developed grains per incident neutron is impossible. While it is feasible to model the number of electrons produced and transported into the film, establishing a link between the number of electrons and the number of exposed grains is impractical. Doing so would require knowledge of the silver bromide grain size, shape, and dispersion, amounts of silver sulfide in each crystal, and some model of the chemical reactions which produce the developed film. These factors

are all proprietary. Even tedious counting of exposed grains under a microscope would not provide a reliable measure of the electron to exposed grain conversion efficiency because it would require accurate knowledge that a crystal had been exposed by multiple electrons. Therefore, the efficiency of this device is better characterized by the location and slope of the useable region. A threshold fluence of $10^{7.154}$ n/cm^2, or 1.427×10^7, is required, based on the first recorded data point above background. Given that the slope is 0.214 ± 0.022 density units per decade, and the resolution of the densitometer used (0.02 density units), the detector mechanism can distinguish between fluences with logarithms differing by 0.08 to 0.10. Taking a 0.1 decade error as illustrative, this would correspond to a relative error of fluence on a linear scale between +25.8% and -20.6%. It must be noted that the detector threshold is dependent on the neutron flux; if the assumed flux of 4514 n/cm^2·s is inaccurate, the threshold will change. However, the detector resolution will remain the same, as the slope on a logarithmic plot will be unaffected.

Aside from film performance, two unexpected problems arose with film handling and development. Many of the low exposure films exhibited developing marks, which were impossible to predict and completely damaged the film, as in Figure 23. These marks resulted in densities differing by up to 0.2 density units. No pattern was identified which caused these patterns.

Figure 23 – Striations apparent in a low (100 s) exposure film.

Residual developing chemicals on six of the films reacted with aluminum foil and supplied packaging used to store them and caused irreparable damage, as shown in Figure 24 below. Developed films were also sensitive to water, which appeared to destroy the film's protective layer. Both of these occurrences were unforeseen, and it is difficult to rule out the possibility of other unanticipated film damage mechanisms.

Figure 24 – A developed film destroyed by contact with aluminum.

V. Conclusions

While the detectors did not perform to the standards desired, they did provide a proof of principle for this detection mechanism. Film density can be a measure of thermal neutron fluence. However, this particular mechanism suffers from problems of repeatability and measurement stability.

5.1 Effectiveness

A few of the design goals were met. The detectors are easily constructed and entirely passive. The exposed films are stable against further radiation once developed, and information contained in the latent image is stable over time. After development, the films provide a permanent record. Finally, the detectors are very economical. Each assembly, including the gadolinium oxide, film, aluminum, Mylar, and BPI, was approximately $20. Only the aluminum foil and film were not reusable, making the cost of each measurement after initial construction only $1.20. Processing was free; if this were not provided, the cost of each measurement would be less than $1.50.

While the detector method met the design goals, it failed three of the four experimental qualifications established in Section 1.2, namely: film response was not reproducible between equal fluence, the minimum detectable fluence was much greater than 1000 n/cm^2, and the uncertainty in any fluence predictions based on a measurement of film darkness was greater than 10%.

The concept of using the BPI to distinguish between direct and scattered neutrons appears to be useful only when the ratio of direct to scattered neutrons is very large; when the detector is in the presence of a large fraction of scattered neutrons, as with the graphite pile, the BPI cannot be used to quantify the ratio. The derivation of the equations in Table 2 assumes that the shadow of the far boron disk is distinguishable from the rest of the image. When this is not true, as in the case of high scattered neutron contribution, the equations fail. The geometry of the BPI is such that neutrons less than 33 degrees from the normal vector are considered direct. [12] The only way to expand this cone would be to have a much wider disk of boron, which would inevitably obscure the entire sensitive region. Therefore the BPI is unsuitable for this application. If this research were repeated, or an application existed where quantifying film exposure contribution from different sources was necessary, a highly collimated thermal neutron beam would be needed. This could be accomplished by constructing a collimator of a small diameter and placing the detector far away, such that the ratio of distance from the source to collimator diameter (the L/D ratio) was greater than 50. This is based on the best practices recommended in [4]. The collimator could be constructed of a drilled piece of polyethylene, or a reservoir of gadolinium oxide with a centered hole. It must be noted that this configuration would greatly reduce the flux, and result in enormously high irradiation times to achieve the fluences used here.

This method necessitates a calibration for different films or developing methods. Other repetitions of this research elsewhere would most likely observe different thresholds and slopes. It cannot be generalized to provide a curve of density versus exposure for any film type and any developing conditions.

Another downfall of this method was that although the data in the films were inherently stable, the films themselves were susceptible to damage during development and storage. This unavoidable uncertainty prevents this method from yielding consistent and accurate results. While these marks were observed only in low exposure films, this may be because changes in film density were easier to quickly observe at low density, since density is a logarithmic quantity. At higher densities, developing marks may have been present, but not immediately identifiable.

The films are inherently sensitive to chemicals in order to be developable. This sensitivity renders the films susceptible to a variety of substances encountered during testing and storage, which irreparably obscures the data point. Data redundancy is absolutely critical, and in many applications, such as neutron detection in a single location during a single and unique NIF shot, this is unacceptable.

5.2 Way Forward

It appears that this method of measurement is not a viable one for the original intent. The film is not nearly sensitive enough to be practical. The method may be improved by the use of gadolinium foil rather than gadolinium oxide. This would negate the need for an intervening Mylar layer, and allow a greater portion of electrons to reach the film. However, this would decrease the number of absorbed neutrons, unless a very thick foil were used. This would also abandon the clear benefits of gadolinium oxide; namely, price and chemical stability.

Although the developing system was standardized, film development nonetheless showed some inconsistencies. The films were also sensitive to some unanticipated factors during storage. These both produced visibly noticeable blemishes on the films. It is reasonable to conclude that other environmental and developmental factors produce similar changes to the films which are not as readily apparent but still affect density measurements. To be viable, development issues causing problems as seen in Figure 23 would need to be identified and prevented, and testing conducted to ensure that storage conditions do not affect film density.

A few advantages of this technique remain. Despite its failures, it is cheap and rugged. Though not experimentally proven here, other work predicts that the device will respond differently to neutrons entering from the rear and from the front. [5] By increasing the thickness, as done here, this conceivably allows for directional discrimination. This could be useful as a means of detecting nuclear material in shipping containers. If the threshold were somehow lowered two or more orders of magnitude, devices could be dispersed through a container, and a certain threshold darkening could confirm the presence of neutrons emitted from a source and then moderated by the shipping container's contents. It could also be used for extremely high thermal neutron fluences where traditional measurement methods may be damaged. This notwithstanding, the method is not suitable for NIF measurements.

Appendix A: Scanned Images of Sample Films

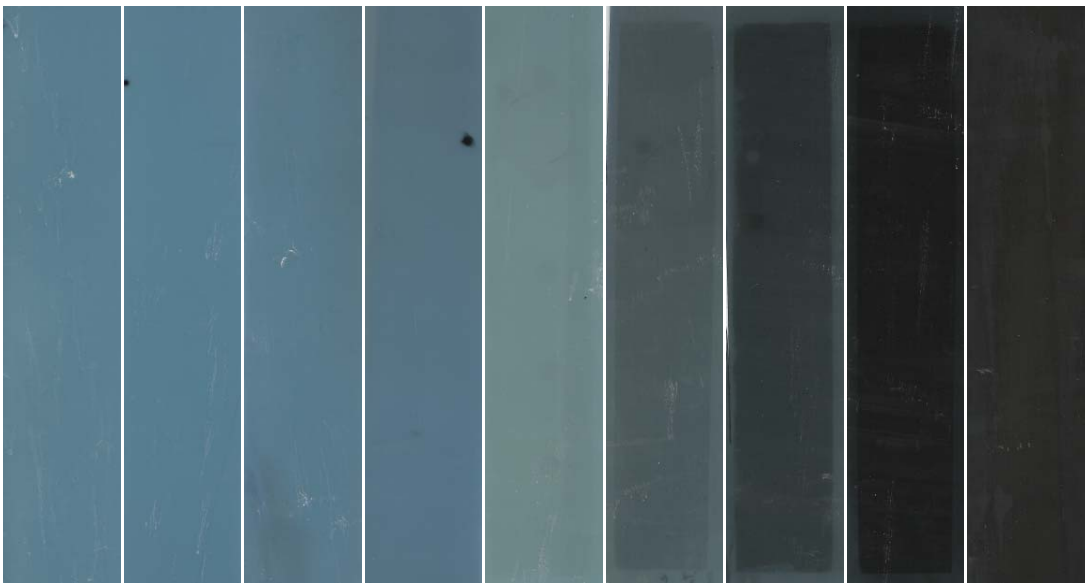

A B C D E F G H I

Figure 25 – Images of exposed films.

Table 9 – Data for Films Shown in Figure 25

	A	B	C	D	E	F	G	H	I
Target Exposure (s)	0	10^2	$10^{2.5}$	10^3	$10^{3.5}$	10^4	$10^{4.5}$	10^5	$10^{5.5}$
Actual Time (DD:HH:MM:SS)	0	1:40	5:16	16:40	52:42	2:40:00	8:47:03	1:3:36:24	3:15:50:25
Uncertainty (s)	-	40	40	40	40	40	40	40	40
Fluence (n/cm^2)	-	4.5×10^5	1.4×10^6	4.5×10^6	1.4×10^7	4.3×10^7	1.4×10^8	4.5×10^8	1.4×10^9
Fluence Uncertainty (%)	-	40	13	6.5	5.3	5.2	5.2	5.2	5.2

Appendix B: Raw Measurement Data

Table 10 – Raw Data from Background Films

	Point 1	Point 2	Point 3	Point 4	Point 5
Film 1	0.96	0.82	0.85	0.8	0.8
Film 2	0.63	0.79	0.66	0.65	0.77
Film 3	0.67	0.68	0.67	0.73	0.66
Film 4	0.83	0.68	0.77	0.76	0.76

Table 11 – Raw Data from Irradiated Films

Film Identification	Location	Point 1	Point 2	Point 3	Point 4	Point 5
1:40-1	Discarded due to markings					
1:40-2	Center	0.69	0.72	0.62	0.67	
	Left	0.66	0.7	0.65	0.66	0.64
	Right	0.65	0.66	0.66	0.66	0.68
	Top	0.66	0.66	0.66	0.66	0.67
	Down	0.64	0.65	0.65	0.65	0.68
	Off Reservoir	0.68	0.66	0.66	0.67	0.66
5:16-1	Discarded due to markings					
5:16-2	Center	0.65	0.67	0.7	0.7	0.67
	Left	0.67	0.66	0.65	0.65	0.67
	Right	0.64	0.66	0.68	0.65	0.66
	Top	0.65	0.66	0.68	0.67	0.67
	Down	0.67	0.66	0.67	0.65	0.67
	Off Reservoir	0.63	0.64	0.66	0.68	0.66
16:40-1	Center	0.69	0.71	0.68	0.7	0.68
	Left	0.66	0.66	0.68	0.66	0.69
	Right	0.68	0.67	0.69	0.68	0.7
	Top	0.63	0.63	0.66	0.67	0.7
	Down	0.64	0.68	0.66	0.67	0.68
	Off Reservoir	0.62	0.68	0.67	0.69	0.68
16:40-2	Center	0.62	0.6	0.65	0.62	0.67
	Left	0.63	0.65	0.62	0.65	0.62
	Right	0.67	0.63	0.64	0.64	0.65

Film Identification	Location	Point 1	Point 2	Point 3	Point 4	Point 5
	Top	0.66	0.65	0.65	0.67	0.62
	Down	0.63	0.63	0.54	0.58	0.65
	Off Reservoir	0.68	0.67	0.66	0.64	0.59
16:40-3	Center	0.59	0.64	0.62	0.64	0.64
	Left	0.62	0.62	0.67	0.62	0.61
	Right	0.61	0.64	0.6	0.6	0.62
	Top	0.62	0.62	0.62	0.62	0.63
	Down	0.65	0.59	0.62	0.59	0.64
	Off Reservoir	0.62	0.59	0.58	0.59	0.63
16:40-4	Center	0.57	0.63	0.63	0.63	0.6
	Left	0.61	0.61	0.63	0.7	0.7
	Right	0.63	0.62	0.65	0.65	0.66
	Top	0.6	0.6	0.61	0.68	0.71
	Down	0.6	0.65	0.64	0.65	0.73
	Off Reservoir	0.64	0.64	0.67	0.68	0.68
52:42-1	Center	0.94	0.99	0.98	1.01	0.71
	Left	0.96	0.98	0.98	0.96	0.97
	Right	0.98	0.98	0.97	0.98	0.96
	Top	0.95	0.96	0.94	0.98	0.95
	Down	0.94	0.97	0.96	0.95	0.99
	Off Reservoir	0.94	0.96	0.93	0.95	0.97
52:52-2	Center	0.91	0.83	0.83	0.89	0.95
	Left	0.9	0.88	0.9	0.9	0.83
	Right	0.93	0.89	0.89	0.91	0.89
	Top	0.94	0.96	0.93	0.93	0.89
	Down	0.88	0.84	0.84	0.86	0.91
	Off Reservoir	0.85	0.85	0.83	0.83	0.87
2:40:00-1	Center	1.1	1.09	1.04	1.11	0.84
	Left	1.04	1.07	1.04	1.04	1.08
	Right	1.02	1.12	1.07	1.08	1.07
	Top	1.02	1.06	1.07	1.06	1.08
	Down	1.02	1.05	1.02	1.03	1.08
	Off Reservoir	0.98	1	0.97	0.99	1.03
2:40:00-2	Center	1.01	1.01	1.05	1.1	1
	Left	1.01	1.02	1.03	1.07	1.09
	Right	1.05	1.02	1.05	1.09	1.05
	Top	0.99	1.07	1.06	1.06	1.09
	Down	1.03	1.04	1.07	1.12	1.08

Film Identification	Location	Point 1	Point 2	Point 3	Point 4	Point 5
	Off Reservoir	0.94	0.96	0.98	1.03	1.08
8:47:03-1	Center	1.21	1.25	1.24	1.29	1.01
	Left	1.23	1.23	1.24	1.29	1.29
	Right	1.21	1.24	1.3	1.29	1.33
	Top	1.24	1.23	1.3	1.35	1.31
	Down	1.19	1.23	1.24	1.29	1.33
	Off Reservoir	1.08	1.14	1.16	1.18	1.25
8:47:03-2	Center	1.26	1.31	1.32	1.33	1.22
	Left	1.29	1.33	1.28	1.32	1.3
	Right	1.32	1.26	1.28	1.35	1.29
	Top	1.23	1.3	1.32	1.31	1.33
	Down	1.2	1.3	1.29	1.27	1.36
	Off Reservoir	1.07	1.13	1.07	1.14	1.31
1:3:30:00-1	Center	1.78	1.76	1.84	1.9	1.13
	Left	1.69	1.7	1.77	1.95	1.93
	Right	1.71	1.8	1.91	1.89	1.94
	Top	1.73	1.79	1.89	1.97	1.93
	Down	1.71	1.76	1.83	1.94	1.94
	Off Reservoir	1.44	1.46	1.49	1.62	1.94
1:3:30:00-2	Center	1.77	1.83	1.89	1.95	1.59
	Left	1.73	1.79	1.87	1.89	1.96
	Right	1.79	1.84	1.93	1.95	1.94
	Top	1.77	1.81	1.91	2	1.94
	Down	1.76	1.85	1.91	1.95	1.95
	Off Reservoir	1.54	1.57	1.6	1.58	1.97
1:3:36:24-3	Center	1.8	1.9	1.94	1.98	1.6
	Left	1.8	1.87	1.88	1.98	1.98
	Right	1.81	1.9	1.91	1.93	1.98
	Top	1.79	1.88	1.85	1.97	1.98
	Down	1.76	1.84	1.88	2	1.93
	Off Reservoir	1.35	1.39	1.44	1.55	1.93
1:3:36:24-4	Center	1.78	1.89	1.89	1.99	1.56
	Left	1.8	1.88	1.89	2	2.04
	Right	1.83	1.86	1.91	2.01	2.04
	Top	1.77	1.9	1.87	2.02	2.05
	Down	1.76	1.8	1.81	1.97	2.02
	Off Reservoir	1.55	1.61	1.63	1.73	1.99
87:50:25-1	Center	2.45	2.48	2.59	2.8	1.77

Film Identification	Location	Point 1	Point 2	Point 3	Point 4	Point 5
	Left	2.51	2.55	2.63	2.74	2.8
	Right	2.47	2.53	2.63	2.77	2.79
	Top	2.51	2.47	2.6	2.92	2.86
	Down	2.46	2.52	2.58	2.83	2.84
	Off Reservoir	1.73	1.77	1.77	1.88	2.79
87:50:25-2	Center	2.55	2.62	2.68	2.9	1.92
	Left	2.56	2.6	2.68	2.78	2.92
	Right	2.57	2.6	2.75	2.87	2.96
	Top	2.49	2.54	2.6	2.72	2.9
	Down	2.52	2.52	2.62	2.87	2.86
	Off Reservoir	2.15	2.23	2.3	2.41	2.92
87:47:03-1	Center	2	2.07	2.26	2.14	2.51
	Left	2.01	2.02	2.05	2.13	2.21
	Right	2.03	2.07	2.07	2.16	2.21
	Top	2.03	2.04	2.03	2.16	2.17
	Down	2.2	2.19	2.13	2.15	2.16
	Off Reservoir	1.77	1.93	1.85	1.89	2.11
87:47:03-2	Center	1.99	2.01	2.03	2.09	2.01
	Left	1.97	2.04	2.01	2.05	2.05
	Right	2.03	2.03	2.02	2.08	2.13
	Top	2	2.06	2.03	2.08	2.1
	Down	1.95	2.04	1.96	2.05	2.08
	Off Reservoir	1.65	1.76	1.74	1.82	2.07

Bibliography

[1]. National Ignition Facility. "What is NIF?" 18 December 2012. https://lasers.llnl.gov/multimedia/publications/pdfs/pk_what_is_nif.pdf.

[2]. Datte, Phil. Researcher at the NIF. Personal Correspondence. September 2012.

[3]. Bickley, Abigail A., Demaree, Grant K., McClory, John W., Miller, William H., Oakes, Thomas M., and Petrosky, James C. "Design Optimization of a Layered Boron Based Solid State Neutron Spectrometer," *2011 IEEE Nuclear Science Symposium Conference Record,* November 2011.

[4]. Domanus, J.C. *Practical Neutron Radiography*. Norwell MA: Kluwer Academic Publishers, 1992.

[5]. Tyufyakov, N.D. and Shtan, A.S. *Principles of Neutron Radiography (Osnovy Neitronnoi Radiographii)*. Moscow: Atomizdat Publishers, 1975.

[6]. Harms, A.A., Blake, T.G., and Marton, J.P. "Neutron Imaging with Thin Gadolinium Converters," *Nuclear Instruments and Methods*, 109: 253-255 (June 1973).

[7]. Hawkesworth, M. R. "Radiography with Low Intensity Neutron Beams: Some Reciprocity Failure Characteristics of Films Used with Light-Emitting Intensifying Screens," *Journal of Scientific Instruments*, 2: 673-678 (August 1969).

[8]. Hawkesworth, M. R. "Films for Neutron Radiography: An Investigation of Film-Intensifying Screen Image Recorders," *Journal of Scientific Instruments*, 2: 235-242 (March 1969).

[9]. *Standard Practice for Fabrication of the Neutron Radiographic Beam Purity Indicators*, ASTM Standard E2003-10, 2010.

[10]. *Standard Test Method for Determining Image Quality in Direct Thermal Neutron Radiographic Examination*, ASTM Standard E545-05, 2010.

[11]. Lima, Clara Tereza dos Santos. *Domestic Conversion Screens of Gadolinium for Neutron Radiography (Tela Conversora Nacional de Gadolinio Para Neutrongrafia)*. MS Thesis. Alberto Luiz Coimbra Institute, Rio de Janeiro Brazil, 2005.

[12]. Newacheck, R. L. *Theory of Operation and Accuracy of the ASTM Neutron Radiography IQI System.* San Ramon CA. Aerotest Operations, Incorporated, Undated.

[13]. Krane, K.S. *Introductory Nuclear Physics*. New York: John Wiley and Sons, 1988.

[14]. Knoll, Glenn. *Radiation Detection and Measurement* (3rd edition). Hoboken NJ: John Wiley and Sons, 2000.

[15]. Stewart, L. "Neutron Spectrum and Absolute Yield of a Plutonium Beryllium Source," *Physical Review,* 98: 740-743 (May 1955).

[16]. McHale, Stephen. Class notes, NENG 651, Introductory Nuclear Physics. School of Engineering and Management, Air Force Institute of Technology, Wright-Patterson AFB OH, November 2011.

[17]. AF NETF Graphite Standard Pile, USAF Technical Report No. WADD-TR-61-174, March 1962.

[18]. National Nuclear Data Center. "Chart of the Nuclides." 12 December 2012. http://www.nndc.bnl.gov/chart.

[19]. Bevins, James. "Calibration of the Graphite Pile at AFIT to Account for Am Ingrowth in PuBe Source". *ANS Presentation*. 1 March 2009.

[20]. De Laeter, J.R., Bohlke, J.K., De Bievre, P., Hidaka, H., Peiser, H.S., Rosman, K.J.R., and Taylor, P.D.P. "Atomic Weights of the Elements: Review 2000," *Pure and Applied Chemistry*, 75: 683-800 (2003).

[21]. National Nuclear Data Center. "Evaluated Nuclear Data File." 14 December 2012. http://www.nndc.bnl.gov/exfor/endf00.jsp.

[22]. Reich, C.W. "Nuclear Data Sheets for A=156," *Nuclear Data Sheets*, 113: 2537-2840 (November 2012).

[23]. Helmer, R.G. "Nuclear Data Sheets for A=158," *Nuclear Data Sheets*, 101: 325-519 (March 2004).

[24]. Harms, A.A. and McCormack, G. "Isotopic Conversion in Gadolinium-Exposure Neutron Imaging," *Nuclear Instruments and Methods*, 118: 583-587 (June 1974).

[25]. Turner, J.E. *Atoms, Radiation, and Radiation Protection*. Weinheim Germany: Wiley-VCH, 2007.

[26]. International Commission on Radiation Units and Measurements. *Stopping Powers for Electrons and Positrons*. ICRU Report 37. Bethesda MD, 1984.

[27]. Garside, B.K. and Harms, A.A. "Detection Process in Neutron Radiography," *Journal of Applied Physics*, 42: 5161-5167 (November 1971).

[28]. Young, J.R. "Dissipation of Energy by 2.5-10 keV Electrons in Al2O3," *Journal of Applied Physics*, 28: 524-525 (May 1957).

[29]. Grafix Plastics. "Mylar Film and Sheet Properties." 10 December 2012. http://www.grafixplastics.com/mylar_prop.asp.

[30]. *Industrial Radiography Image Forming Techniques.* General Electric Inspection Technologies, 2007.

[31]. McKinney, William. "Radiographic Film Development" in *Nondestructive Testing Handbook, Volume 4: Radiographic Testing* (3rd Edition). Columbus OH: American Society for Nondestructive Testing, Incorporated, 2002.

[32]. Lewis, Bill. Chair, ASTM E-07.05 Subgroup of Neutron Radiography Standards. Personal Correspondence. 1 November 2012.

[33]. Lima, C.T.S, Crispim, V.R., and Santos, W.M.S. "Gadolinium Sheet Converter for Neutron Radiography," *Applied Radiation and Isotopes*, 65: 1381-1385 (June 2007).

[34]. Schwarzschild, K. "On the Deviations from the Law of Reciprocity for Bromide of Silver Gelatin," *The Astrophysical Journal*, 11: 89-91 (1900).

[35]. NIST Center for Neutron Research. "Neutron Scattering Lengths and Cross Sections." 18 December 2012. http://www.ncnr.nist.gov/resources/n-lengths/.

[36]. ESPI Metals. "Gadolinium MSDS." 18 December 2012. http://www.espimetals.com/msds's/Gadolinium.htm.

[37]. NIST Center for Neutron Research. "Scattering Length Density Calculator." 7 January 2013. http://www.ncnr.nist.gov/resources/sldcalc.html.

[38]. VWR Lab Shop. "Reynolds Wrap Aluminum Foil." 20 December 2012. http://vwrlabshop.com/reynolds-wrap-aluminum-foil/p/0014244/.

[39]. FoodSaver Customer Service. Personal Correspondence. 12 November 2012.

REPORT DOCUMENTATION PAGE		Form Approved OMB No. 0704–0188
The public reporting burden for this collection of information is estimated to average 1 hour per response, including the time for reviewing instructions, searching existing data sources, gathering and maintaining the data needed, and completing and reviewing the collection of information. Send comments regarding this burden estimate or any other aspect of this collection of information, including suggestions for reducing this burden to Department of Defense, Washington Headquarters Services, Directorate for Information Operations and Reports (0704–0188), 1215 Jefferson Davis Highway, Suite 1204, Arlington, VA 22202–4302. Respondents should be aware that notwithstanding any other provision of law, no person shall be subject to any penalty for failing to comply with a collection of information if it does not display a currently valid OMB control number. PLEASE DO NOT RETURN YOUR FORM TO THE ABOVE ADDRESS.		
1. REPORT DATE (DD–MM–YYYY) 22-03-2013	2. REPORT TYPE Master's Thesis	3. DATES COVERED *(From — To)* 01-06-2012 – 11-03-2013
4. TITLE AND SUBTITLE Passive, Low Cost Neutron Detectors for Neutron Diagnostics at the National Ignition Facility		5a. CONTRACT NUMBER 5b. GRANT NUMBER 5c. PROGRAM ELEMENT NUMBER
6. AUTHOR(S) Loyd, Nathaniel C., 1st Lt, USAF		5d. PROJECT NUMBER 5e. TASK NUMBER 5f. WORK UNIT NUMBER
7. PERFORMING ORGANIZATION NAME(S) AND ADDRESS(ES) Air Force Institute of Technology Graduate School of Engineering and Management (AFIT/ENY) 2950 Hobson Way WPAFB OH 45433-7765		8. PERFORMING ORGANIZATION REPORT NUMBER AFIT-ENP-13-M-23
9. SPONSORING / MONITORING AGENCY NAME(S) AND ADDRESS(ES) Dr. Brett Bedeaux USAF Nuclear Weapons Center 498 NSW/NWASA 1551 Wyoming Blvd SE Kirtland AFB, NM 87117		10. SPONSOR/MONITOR'S ACRONYM(S) AFNWC 11. SPONSOR/MONITOR'S REPORT NUMBER(S)
12. DISTRIBUTION / AVAILABILITY STATEMENT APPROVED FOR PUBLIC RELEASE; DISTRIBUTION UNLIMITED		
13. SUPPLEMENTARY NOTES This material is declared a work of the U.S. Government and is not subject to copyright protection in the United States.		
14. ABSTRACT Experimental validation of neutron fluence models of fusion events at the National Ignition Facility is necessary to predict radiation damage to measurement electronics. Due to programmatic and facility limitations, traditional neutron measurement techniques are not well suited for this application. Notably, a low cost and passive measurement technique that provides a permanent record is preferred. A detector was designed using gadolinium oxide contained within an aluminum reservoir. The reservoir is secured by a thin layer of Mylar and x-ray film, and vacuum sealed in a light tight package. In the presence of a thermal neutron flux, the gadolinium atoms absorb incident neutrons and partially de-excite by conversion electron emission. The conversion electrons exit the gadolinium oxide layer, penetrate the Mylar, and expose the x-ray film. After developing the film, the film exposure is quantified and directly related to the neutron fluence. The configuration was sensitive to thermal neutron fluences between 1.43×10^{7} and 1.43×10^{9} n/cm^{2}, and could distinguish between fluences differing by more than a tenth of a decade.		
15. SUBJECT TERMS Thermal Neutrons, Gadolinium Oxide, X-Ray Film		

16. SECURITY CLASSIFICATION OF:			17. LIMITATION OF ABSTRACT	18. NUMBER OF PAGES	19a. NAME OF RESPONSIBLE PERSON Dr. John McClory, AFIT/ENP
a. REPORT U	b. ABSTRACT U	c. THIS PAGE U	UU	103	19b. TELEPHONE NUMBER (Include Area Code) (937)255-3636, ext 7308

Standard Form 298 (Rev. 8–98)
Prescribed by ANSI Std. Z39.18